Investigation of Optimal Control Strategies for an Indirect Solar Assisted Heat Pump (i-SAHP) System

W. Youssef , Y.T. Ge

Centre for Sustainable Energy Use in Food Chains, School of Engineering and Design
Brunel University, Uxbridge, Middlesex, UB8 3PH, UK
Corresponding author: Yunting.Ge@brunel.ac.uk ,Walid.Youssef@brunel.ac.uk

Abstract
In this paper, a constructed i-SAHP test rig is methodically illustrated with recommended control logic that can be applied to the system. The i-SAHP rig consists of three circulating loops in which the solar thermal and heat pump loops are the heating sources for a solar storage tank. The third loop is a load imitating loop to emulate a load profile in a typical UK residential house. The whole system is automatically controlled by a Building Management System (BMS) with special designed control strategies to maintain a constant storage tank water temperature during 24 hours operational period. Sequence controls and operations of solar and heat pump loops at a designed load profile and instantaneous weather conditions are included. In addition, the safety operations of the system are also considered. The test rig with the designed control strategies are operated continuously for at least 48 hours to verify the applicability and efficiency of the controls. The measurements are thus evaluated, compared and analysed so as to achieve further optimisation of the control strategies.

1 Introduction

Running out of non- renewable energy sets a solar thermal system one of the most important applications for producing domestic hot water and space heating nowadays. In the UK, up to 30% of national energy is used for the purposes of space heating and domestic hot water through the direct burning of fossil fuels, in particular natural gas. The use of the heat pump has developed and become more effective for the last 30 years [1]. In addition, the development of solar thermal system has been found to be an important area for further investigations [2]. Economic study proved that the use of an indirect Solar Assisted Heat Pump (i-SAHP) system controlled by Building Management System (BMS) could be a more feasible option considering important factors such as cost, application area limitation, constant water heating production, high efficiency and internet access and operation. Considering that the victorious designs of SAHPs are mostly liquid to liquid types with thermal storages[3], many studies have been carried out in order to classify the optimal SAHP system operations. J. Duomarco found that the optimal SAHP was one that could generate heating with less usage of auxiliary energy per unit volume [4]. Decreasing the heat loss from the supply pipes was found to be an interesting area of study to improve the system operation [5]. S. Li et al used another method to optimize the control strategy by developing algorithm for the set point which could save 34% of the system power consumption [6]. L. M. Nhut and Y. C. Park studied the optimal control for thermal solar system and it was found that the variation of water mass flow rate through solar circulating pump had little effect on the solar energy gained but had 65% reduction of the pump power consumption [7]. C.Sebarchievici and I. Sarbu studied the automatic control for ground-coupled heat pump and it was found that the new control strategy could improve the COP by 8% and reduced the CO2 emission by 8% [8]. P. Kepplinger et al studied the optimal control for resistive domestic hot water heaters using linear optimization and it was noted that the saving depended in the first place on user behaviours. With a particular designed user behaviour, it was demonstrated that the system could save 12% of energy by implementing this technique [9]. However, the optimal control strategies in an i-SAHP system need to be further investigated.

In this paper, a test rig of an i-SAHP will be demonstrated and its control strategies have been designed and evaluated by measuring the water temperature inside a storage tank at specified load profiles. In the mean time, some other important operating and energy parameters are also measured and analysed. Further improvement for the control strategies will also be discussed.

2 System description

The test rig of an indirect solar assisted heat pump (i-SAHP) system is shown schematically in Figure. The system is designed to be installed on the roof of a standard UK building. The test rig system consists of a number of main components, as listed in Table. The evacuated tube collector has a total surface area of 3.021 m^2 and 52° tilt angel with south facing which was installed on a building roof outside the rig. The insulated storage tank has a volume of 300L capacity and is made of stainless steel with two coils immersed inside, one for direct solar operation and the other for indirect solar operation. There is also a 43L auxiliary heater tank to protect the circulating water from freezing when the heat pump is in operation. The heat pump using R404a as refrigerant consists of four major components: compressor, evaporator, condenser and expansion valve.

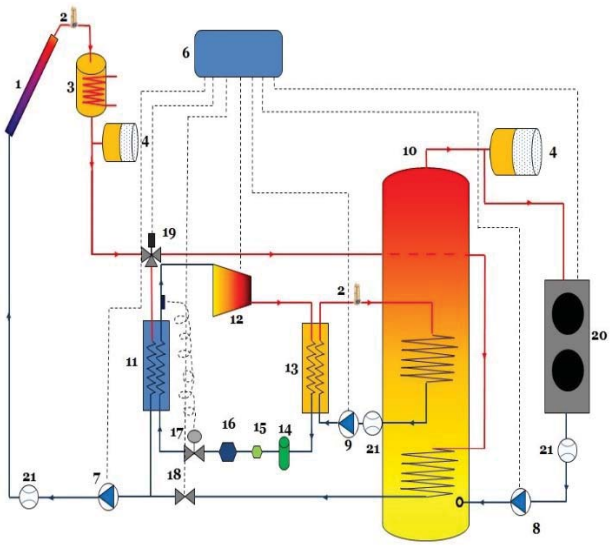

Figure 1: *Schematic diagram of indirect solar assisted heat pump (i-SAHP)*

Table 1: *i-SAHP components list*

1	*Collector*	*12*	*Compressor*
2	*Deaerator*	*13*	*Condenser*
3	*Heater Tank*	*14*	*Receiver*
4	*Expansion Tank*	*15*	*Filter*
6	*Controller*	*16*	*Sight Glass*
7	*Solar Pump*	*17*	*Expansion Valve*
8	*Load simulation Pump*	*18*	*2-way Valve*
9	*HP Pump*	*19*	*3-ways Valve*
10	*Storage Tank*	*20*	*Water Cooler*
11	*Evaporator*	*21*	*Flowmeter*

The operation of the system can be classified into three main loops. The first one is a direct solar loop which is applied to produce fully renewable energy directly from the solar collector to the solar storage tank, similar to any traditional solar thermal system. This loop will work independently if it can obtain solar energy and heat up the storage tank. The second one is an indirect solar loop which is used as an assistant to the heat pump. In this loop, the heating of storage tank water is provided by the heat pump and the solar collector gathers solar energy and uses it as the heat source to the heat pump through its evaporator. This loop will only operate if the direct solar loop is not powerful to provide heating for the water tank. The operations of these two loops are controlled automatically by two motorised valves of 19 and 18 shown in Figure 1. The liquid used in each loop is a mixture of 36% Ethylene Glycol and 64% pure water with freezing temperature of -20°C. The third one is a load loop including an expansion tank, an water cooler and a liquid pump. Since it is hard to implement the experiment in an actual dwelling, the load loop has been purposely constructed in order to simulate and establish a standard UK dwelling hot water consumption profile during a long typical day. Based on the designed load profile, the circulation pump speed is controlled accordingly by an inverter in order to modulate the required feed water flow rate to the storage tank. This can be implemented by controlling the pump motor frequency as it is a direct proportional with water flow rate. In the meantime, as shown in Figure, the feed water temperature at the water cooler outlet is controlled the water cooler's fan speed and is to be maintained at 18 ℃ considering of the average feed supply temperature for a standard dwelling in the UK [10]. The main target of this study is to maintain the outlet temperature from the solar tank at 60℃ by operating separately of the first and 2nd solar loops at a specified load profile.

3 Description of the developed control systems

As shown in Figure 2, the control strategy is selected from a number of applicable methods to the test rig. The main target of this strategy is to maintain the temperature of the water inside the tank at 60℃ ±2°C during a typical hot water consumption day. Therefore, the logic is designed to check firstly if the

temperature inside the tank is below 58°C. If so, it will check if there is a hot water demand based on the occupation schedule of dwelling which in our case is 24 hours continuous operation. When the system is on demand the load simulation pump will be controlled and provide specified hourly water flow rate according to the load profile of a standard dwelling in the UK, as shown in Figure 3. If there is a demand, the logic will check first if there is enough radiation that can produce heat to warm the storage tank. In order to implement that, the difference between the inlet and the outlet of the collector temperatures has to be more than 3°C. If the difference is less than 3°C, the 3-ways valve will direct the flow from the direct solar loop to the indirect solar loop and the 2-way valve will be fully closed.

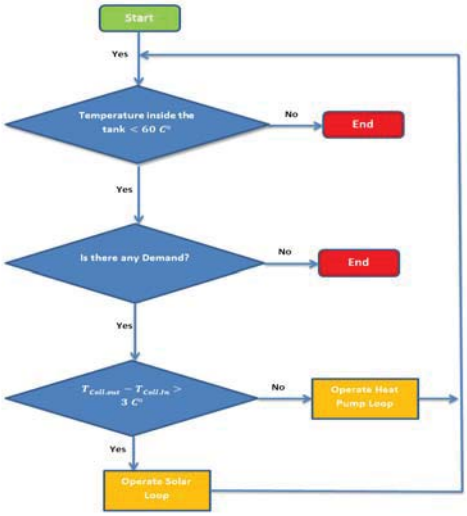

Figure 2: *i-SAHP logic flowchart*

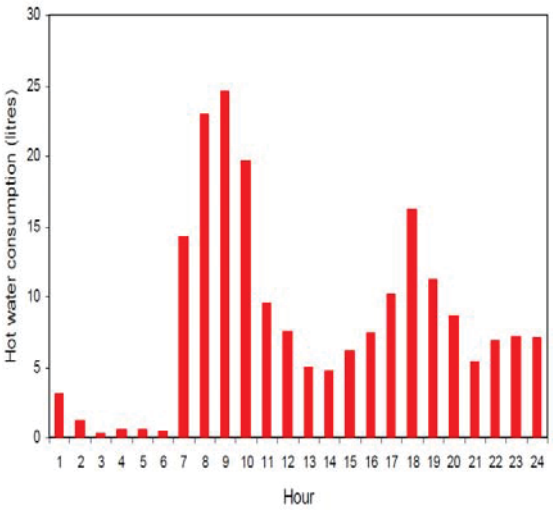

Figure 3: *Hot water consumption for UK dwelling*

To ensure the safety operation of the system, two additional logics have been applied to the test rig to prevent the risks of high pressure in the heat pump compressor and the sudden freeze on the evaporator. The first one is to start the solar circulation pump and condenser side water pump first before starting up the compressor and shut off the compressor first before turning off the pumps The second safety logic is to protect the direct and indirect loops from freezing during winter when heat pump is in use. This logic has implemented by Boolean control of the auxiliary heater of the 43L tank which operate this heater when the temperature of this heater tank outlet drops below -10°C and stops when the temperature rises to 5°C.

4 Control strategy validation

This section will present the test rig experiment results that illustrate the performance of the strategy applied for the control of the indirect solar assisted heat pump which was running for 48 hours during winter period (26th and 27th Feb 2015). Figure 4 shows the outlet temperature to the load during 48 hours operation, which demonstrates that the outlet temperature to the load slight varies during high pick demand at evening. The reason is that the low water consumption profile has maximum pick demand of 25 litres per hour during that time; this is reasonably small compared to the tank volume which can cover higher demand. It is also shown in the graph Figures 5 and 6 that the system operated only three times during these 48 hours.

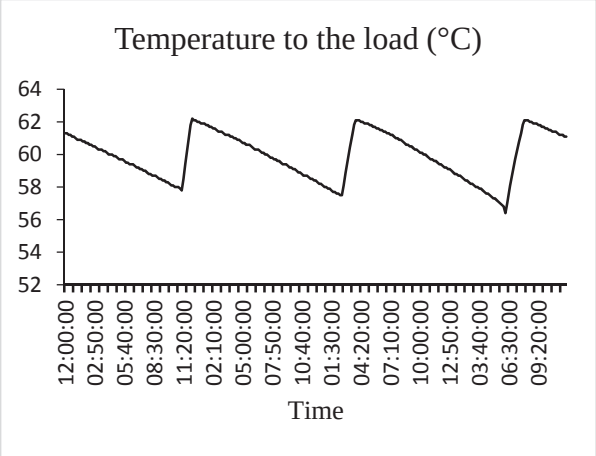

Figure 4: *Temperature to the load in 48 hours operation*

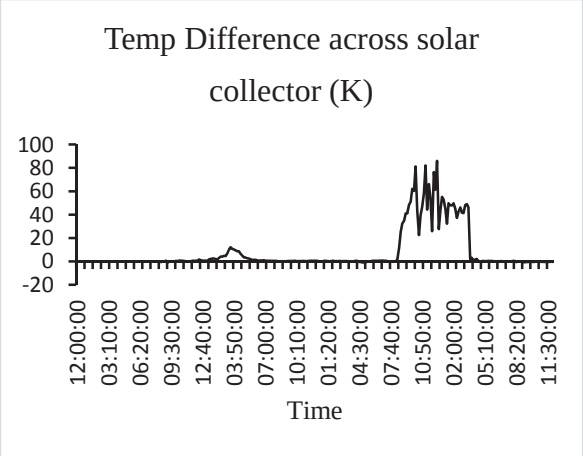

Figure 5: *Temperature difference across the solar collector in 48 hours operation*

The compressor power capacity during 48 hours operation is shown in Figure 6. The compressor capacity was calculated according to the following:

$$W_{Comp} = \dot{m}_{Ref}\left(h_{Comp\ out} - h_{Comp\ in}\right) \quad kW \tag{1}$$

At the beginning of each operation, the heating capacity was found about 0.7 kW then it decreased linearly because the evaporating temperature decreased.

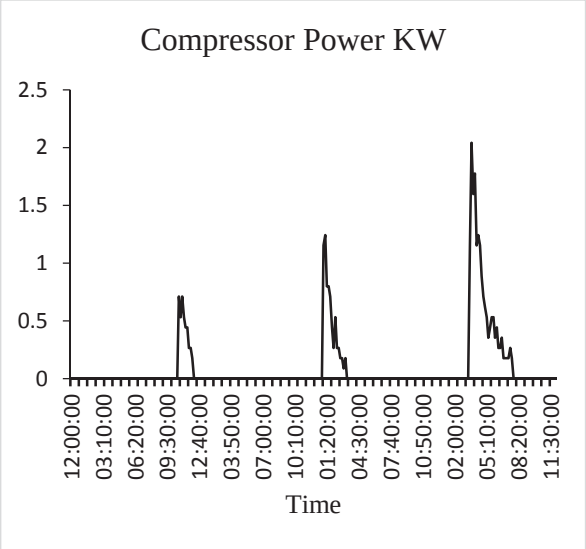

Figure 6: *Compressor power in 48 hours operation*

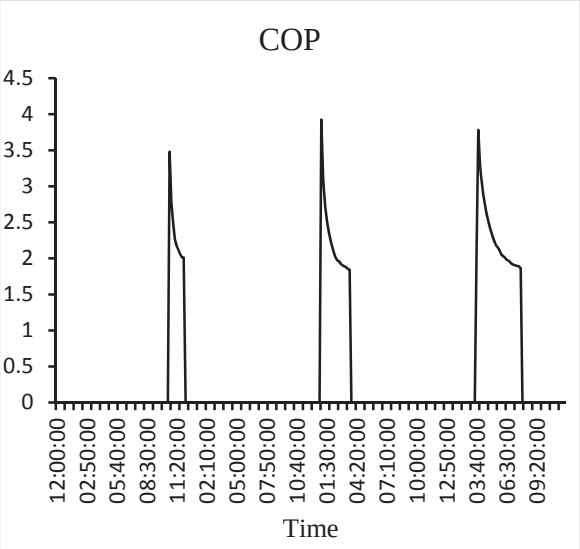

Figure 7: *Heat-Pump COP in 48 hours operation*

The standard COP for this heat pump should be in a range of 1.29 to 3.44 depending on the evaporating temperature. The COP was found to be 3.48 at the beginning for the operation and 2.010 by the end of the operation as shown in Figure 7. The COP was calculated according to the following formula:

$$COP_{HP} = \frac{Q_{Cond}}{W_{Comp}} = \frac{h_{Cond\ in} - h_{Cond\ out}}{h_{Comp\ out} - h_{Comp\ in}} \tag{2}$$

Figure illustrates the temperatures across the evaporator including refrigerant inlet and outlet, water inlet and outlet during the test operation. The refrigerant inlet temperature at this point was -1.7 ℃ at the start of the operation and it dropped to about -3.6 ℃ in the end. The temperature of the refrigerant at evaporator outlet was 8.4 ℃ at the start of the operation and 3.8 ℃ when it finished.

5 Conclusions

CO_2 emission reduction is one of the key research areas of alternative clean energy production with high performance operation, compared to traditional heating systems. Therefore, i-SAHP is a significant area to study as it represents an ideal way of clean heating production. The paper presented the experimental test rig behaviours for 48 hours operation in a typical UK house during winter. The results showed that this system can cover the target demand with very low power consumption. However, it is crucial to implement further experiments on the test rig behaviours in order to cover higher demand to define the system load capacity. As a consequence, an additional investigation will be carried out during a summer day to present the effect of the direct thermal loop and its effect on the system power consumption.

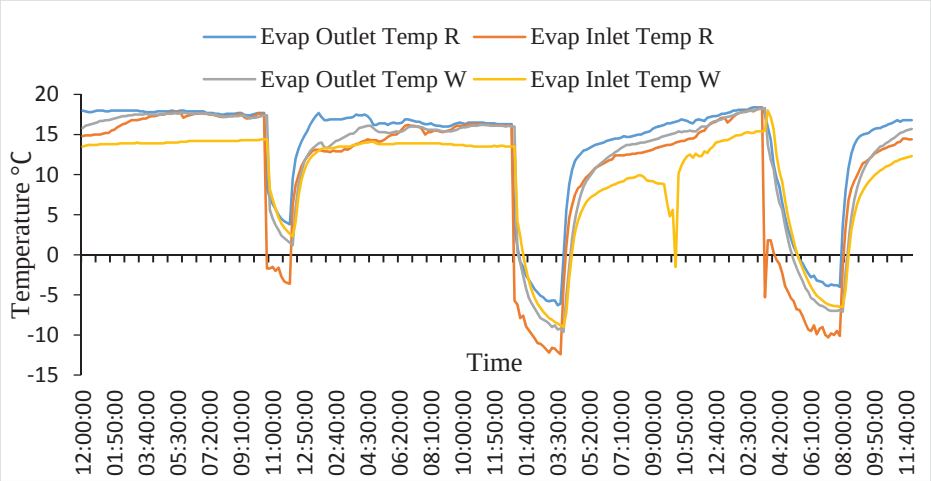

Figure 8: *Refrigerant temperature at evaporator inlet in 48 hours operation*

References

[1] A. Hepbasli and Y. Kalinci, "A review of heat pump water heating systems," *Renew. Sustain. Energy Rev.*, vol. 13, no. 6–7, pp. 1211–1229, Aug. 2009.

[2] S. Sadhishkumar and T. Balusamy, "Performance improvement in solar water heating systems—A review," *Renew. Sustain. Energy Rev.*, vol. 37, pp. 191–198, Sep. 2014.

[3] R. S. Kamel and A. S. Fung, "SOLAR SYSTEMS AND THEIR INTEGRATION WITH HEAT PUMPS: A REVIEW," *Energy Build.*, vol. 87, pp. 395–412, Nov. 2014.

[4] J. L. Duomarco, "Figure of merit for solar domestic hot water systems," *Sol. Energy*, vol. 111, pp. 151–156, Jan. 2015.

[5] L. M. Ayompe and A. Duffy, "Thermal performance analysis of a solar water heating system with heat pipe evacuated tube collector using data from a field trial," *Sol. Energy*, vol. 90, pp. 17–28, Apr. 2013.

[6] S. Li, J. Joe, J. Hu, and P. Karava, "System identification and model-predictive control of office buildings with integrated photovoltaic-thermal collectors, radiant floor heating and active thermal storage," *Sol. Energy*, vol. 113, pp. 139–157, Mar. 2015.

[7] L. M. Nhut and Y. C. Park, "A study on automatic optimal operation of a pump for solar domestic hot water system," *Sol. Energy*, vol. 98, pp. 448–457, Dec. 2013.

[8] C. Sebarchievici and I. Sarbu, "Performance of an experimental ground-coupled heat pump system for heating, cooling and domestic hot-water operation," *Renew. Energy*, vol. 76, pp. 148–159, Apr. 2015.

[9] P. Kepplinger, G. Huber, and J. Petrasch, "Autonomous optimal control for demand side management with resistive domestic hot water heaters using linear optimization," *Energy Build.*, Dec. 2014.

[10] E. S. Trust, "Measurement of domestic hot water consumption in dwellings," *Energy Savings Trust*, 2008.

Experimental Comparison of the Performance of a Waste Heat Recovery Organic Rankine Cycle System for Truck Application Using R245fa and R1233zd

Ludovic Guillaume [a], Arnaud Legros [a], Vincent Lemort [a]

[a] Thermodynamics laboratory, University of Liège, Campus du Sart Tilman, B49, B-4000 Liège, Belgium
* Corresponding author. Email: Ludovic.guillaume@ulg.ac.be; Tel. +32(0)3664823

Abstract
The reduction of CO2 emissions is a strategic goal of the EU where Heavy Duty Vehicles (HDV) can contribute in a relevant way. A very promising solution is to recover the waste heat, which is about 50 to 60% of the combustion energy. Transforming this heat in mechanical or electrical energy will enable to increase the overall energy efficiency of the vehicle. Consequently, the fuel consumption and the CO2 emissions will be reduced.

As being adopted for large stationary applications, the heat re-use can be performed by means of an external combustion engine, such as the Organic Rankine Cycle (ORC), using the waste heat as energy source. However, the adoption of such technology in the automotive domain requires specific R\& D activities to select and develop the components, identify the most appropriate system architecture and integration level so to achieve sustainable cost and the reliability requirements.
A significant part of these activities is devoted to the selection of the expansion machine and working fluid. Within this context, the objective of this study is to compare the performance of an ORC system using a radial turbine and exploiting the waste heat out of a truck for two working fluids: R245fa and R1233zd.

A test rig integrating the turbine was built. This turbine was developed mainly using components of truck turbochargers and was directly coupled to an electrical generator. The waste heat of the exhaust gases and the recirculated gases of the truck were simulated using an electric oil boiler associated with the ORC loop. The electrical power supplied by the turbine, was then dissipated in a load bench while the condenser was cooled by a water loop.

Measurements in steady-state were performed in order to evaluate the performance of the turbine when varying its pressure ratio, its rotational speed and the mass flow rate for various oil temperatures and mass flow rates.

Keywords waste heat recovery; organic Rankine cycle; experimental comparison; R245fa; R1233zd.

1 Introduction

It is now accepted that greenhouse gas emissions from human activities are enhancing the global warming effect keeping the earth at a temperature higher than it would otherwise be [5]. In the last twenty years, the world energy consumption has increased by more than 30% [3] despite the adoption by the United Nations on Climate Change of the Kyoto Protocol [7].

Figure 1 (a) illustrates the situation as it was in 2009 in Europe in terms of CO2 emissions. The transport sector is responsible of about one third of these emissions. And it was pointed out that "*Heavy-Duty Vehicles represent about a quarter of EU road transport CO2 emissions and some 6% of the total EU emissions*" [2].

Despite recent improvements in fuel consumption efficiency, HDV emissions are still rising, mainly because of the increasing number of vehicles in traffic. Nowadays, HDV are the second-biggest source of emissions within the transport sector, i.e. larger than both international aviation and shipping. As a result, the reduction of these CO2 emissions has become a strategic goal of the EU.

"*As part of the EU's future strategy to address HDV fuel consumption and CO2 emissions, a number of actions can be considered that will result in:*

- *improved vehicle efficiency through new engines, materials and design,*
- *cleaner energy use through new fuels and propulsion systems,*
- *better use of networks and more efficient fleet operation, with the support of information and communication systems.*" [2]

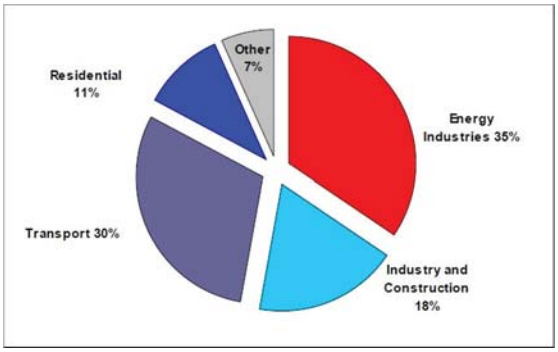

Figure 1(a): *European CO2 emissions by sector in 2009*

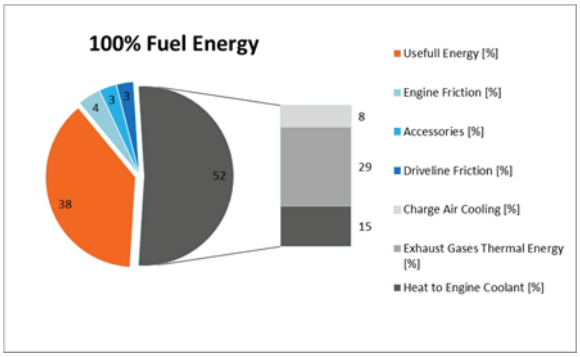

Figure 1(b): *Waste Heat repartition for truck applications*

A very promising solution is the re-use of the waste heat, which is about 50 to 60% of the combustion energy (Figure1 (b)), transforming it into mechanical or electrical energy so to increase the overall vehicle energy efficiency and consequently reducing its CO2 emissions and fuel consumption.

The heat re-use can be performed by means of a thermodynamic cycle (e.g. organic or non-organic Rankine cycles) using the waste heat as energy source as is being adopted for large stationary applications.

The adoption of such technology in the automotive domain requires specific R&D activities to identify the most appropriate system architecture and integration level so to achieve sustainable cost and the reliability requirements. A major part of these activities is dedicated to the selection of the working fluid and the expansion machine. The working fluid selection process has been widely investigated in several studies [4] but no universal optimal fluid is indicated since the choice is highly dependent to the target application. A detailed list of the guidelines and indicators that should be taken into account when selecting an organic fluid for power generation is reported in [6].

In this study, the results of an experimental campaign on an ORC test rig using two different working fluids, R245fa and R1233zd, is presented. The cycle operates between a maximum heat source temperature of 180°C and a minimum heat sink temperature of 10°C. The thermodynamic performance of the different components of the ORC unit for the two fluids are evaluated and compared.

2 Material and methods

A picture and the schematic layout of the ORC test rig are shown in figure 2 (a). The system is a regenerative cycle equipped with a radial turbine characterized by a maximal shaft power of 3.5 kW. This turbine was developed mainly using components of truck turbochargers and was directly coupled to an electrical generator. The bearings are lubricated and the generator is cooled through two by-pass pipes that go from the pump outlet to the turbine as shown in figure 2 (b). The variable speed membrane pump, through the asynchronous generator, was connected to an inverter that allows controlling the rotational speed of the machine. The waste heat of the exhaust gases and the recirculated gases of the truck were simulated using an electric oil boiler associated with the ORC loop. The electrical power supplied by the turbine generator was then dissipated in a load bench while the condenser was cooled by a water loop. A liquid receiver is placed between the condenser outlet and the subcooler inlet. A summary of the main ORC components characteristics is reported in table 1.

Table 1: *Summary of the specifications of the main ORC components*

System Component	Specifications
Evaporator, Condenser, Recuperator	Brazed plate type
Pump	Volumetric membrane pump, 3kW motor, 1500 RPM nom, $P_{max} = 70\ bar$
Expansion machine	Radial turbine

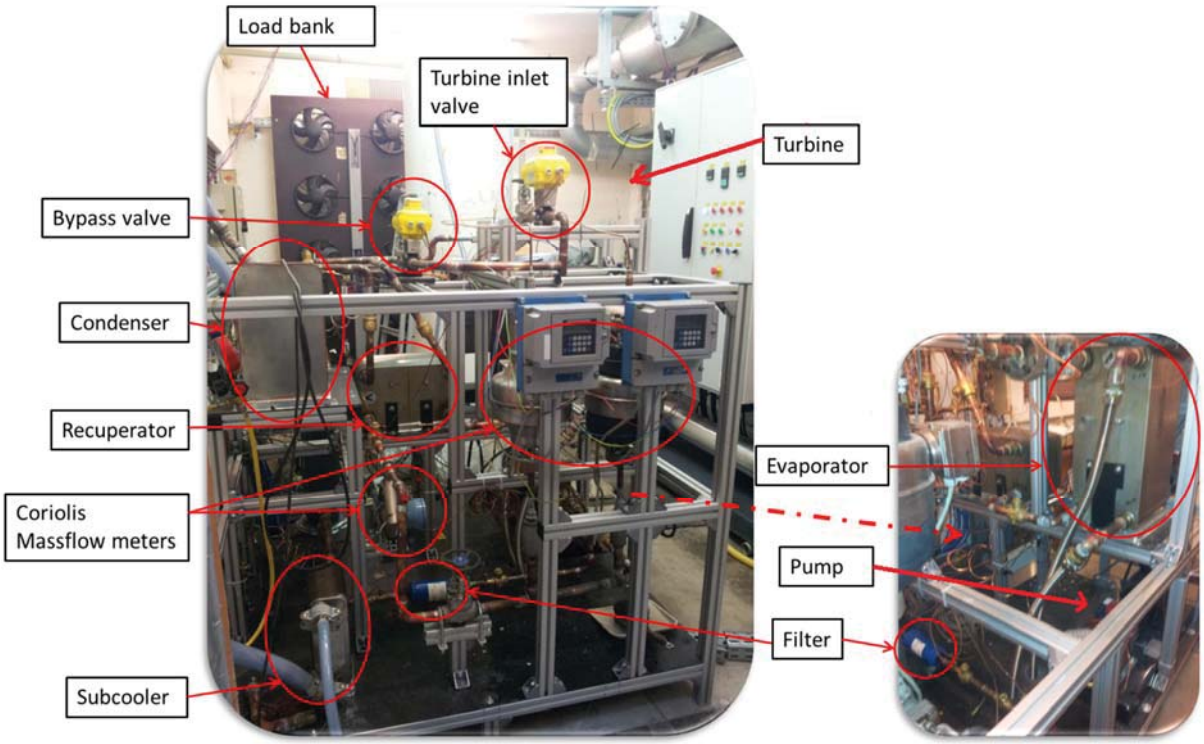

Figure 2(a): *Pictures of the ORC test rig*

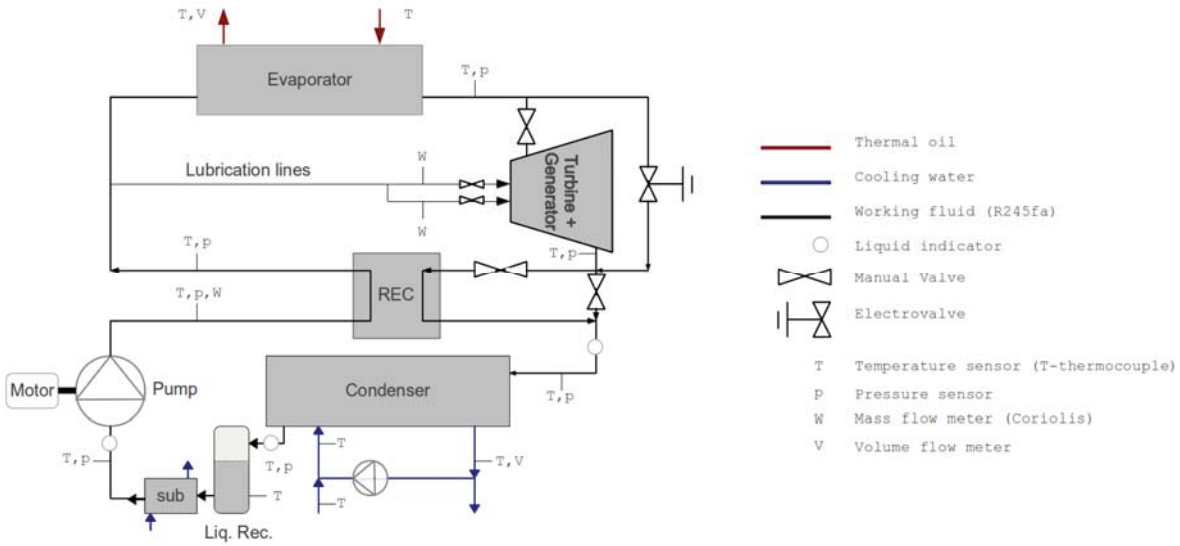

Figure 2(b): *Schematic layout of the ORC test rig*

2.1 Heating and cooling loops

The low-capacity waste heat thermal energy source is represented by means of an electrical boiler where thermal oil, Pirobloc HTF-Basic, is pumped through to temperatures of up to 125°C. The boiler has a maximum power of 250 kWth. A proportional integral (PI) controller is implemented to maintain the

temperature of the oil at the inlet of the evaporator constant during transient in the ORC test rig (e.g. change of ORC pump rotational speed).

A variable flow rate of water is used as heat sink to cool down the working fluid in the condenser (and the subcooler).

2.2 Data acquisition system

Absolute pressure sensors (APS) and Type-T thermocouples at the inlet and at the outlet of the different components allow the determination of the energy balance for each component and the management of the plant. The working fluid mass flow rate is measured by means of a Coriolis flow meter (CFM) installed at the pump outlet. The condenser cooling loop is equipped with two type-T thermocouples to measure the temperature of the cooling fluid at the inlet and at the outlet of the condenser and a water counter is used to measure the flow rate of water. In the heat source circuit, the temperature of the oil is measured at the inlet and at the outlet of the evaporator using type K thermocouples and a high temperature water counter is used to measure the oil mass flow. The turbine electrical power is measured by means of a 3-phases wattmeter. The characteristics of the measurement devices are reported in table 2.

Table 2: *Measurements devices specifications*

Variable	Device type	Studied Range	Uncertainty
Mass flow	Coriolis Flow meter (CFM)	0-0.5 kg/s	±0.1%
T (ORC)	Type-T thermocouples	0-130 °C	±0.5K
T (Heat sink)	Type-T thermocouples	0-70 °C	±0.5K
T (Heat source)	type-k thermocouples	0-180 °C	±1.5K
P	Absolute Pressure Sensors (APS)	0-20 bar	±0.02 bar
El. Power	Wattmeter	0-10 kW	±0.1%

2.3 Working fluid selection

Different studies focus on the characteristics required by the fluid in order to retrieve the highest efficiency or power out of the given thermal energy source [4] [6]. For low quality waste heat recovery, the choice of the working fluid is often restricted to the refrigerant fluid family because of their low critical temperatures and pressures. However, the availability on trucks of high temperature heat sources such as the recirculated gases can also lead to the use of ethanol or water as working fluid.
In the present study, the turbine was designed to operate with the well-known refrigerant R245fa. This fluid has some advantages:

- not toxic,
- not flammable
- easily available on the market
- null Ozone Depletion potential (ODP)

But it is also characterized by a medium Global Warming Potential (GWP=1030) and should therefore gradually disappear.

Thus, in addition to an experimental campaign with R245fa, another campaign was then realized with a probable replacement for R245fa: R1233zd (GWP=6).

2.4 Experimental investigation

Several points were measured for both R245fa and R1233zd. These points were obtained by keeping the system at a stable condition for a minimum of 15 minutes and by averaging the measurements over a period of 2 minutes. Only some of these points are presented here.

The condenser pressure was varied between a value of 2.5 and 4.5 bar for R245fa and between 3 and 4 bar for R1233zd.

The working fluid flow rate is imposed by varying the pump rotational speed, the evaporating pressure is imposed by the turbine. The condensing pressure is imposed by adjusting the cooling flow rate in the condenser.

The rotational speed of the turbine was varied as well as the bearings lubrication flow rate, responsible of windage losses.

Comparing the performance of the ORC systems could be done for same saturation temperature levels of the two fluids. This would enable an objective comparison of both fluids in case of exact same heat sources and heat sinks temperature and mass flow profiles. The result of this comparison would mainly be that the pressure level corresponding to the same saturation temperature is lower for R1233zd than for R245fa. The condensing pressure is therefore reduced but just as the evaporating pressure is reduced. But the latter is much more reduced and so is the pressure ratio and the turbine power production (figure 3).

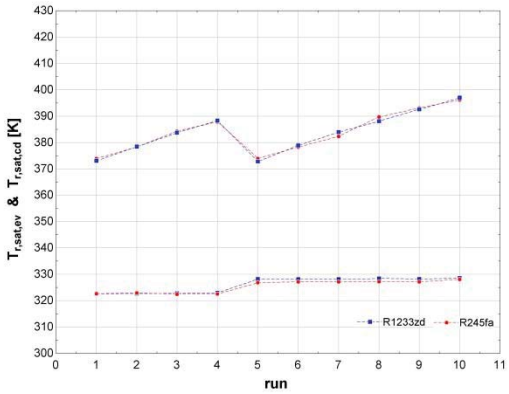

Figure 3(a): *Evaporating and condensing temperature levels for both R245fa and R1233zd*

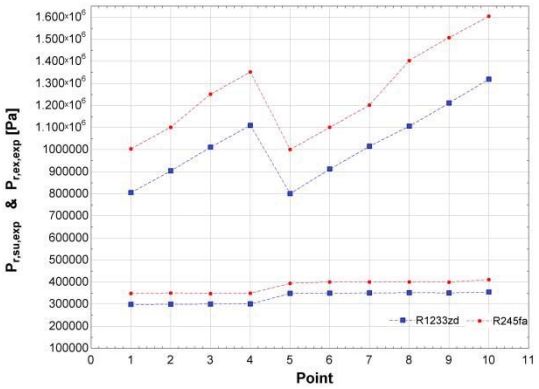

Figure 3(b): *Evaporating and condensing pressure levels for both R245fa and R1233zd*

In this study the performance of the system is compared for same condensing temperature levels and evaporating pressure levels. This enables a comparison more adapted to the WHR on truck application for which the main constraint is generally the condensing temperature because of the mid-to-high temperature of the heat sink. But the evaporating pressure can be optimized and so there is no reason to keep the same temperature levels on the evaporator side.

2.5 Theory / calculation

2.5.1 Thermal Energy Balance

The thermal energy balances over each component of the ORC test rig can be computed in order to check if the first law of thermodynamics is respected. Possible unbalances can indicate measurement issues or unconsidered parasitic phenomena such as ambient losses. The energy balance of a component is calculated as follows:

$$\dot{Q}_{amb} + E_r = \dot{M}_{sf} C_{p,sf} (T_{sf1} - T_{sf2}) - \dot{M}_{wf} (h_{wf,1} - h_{wf,2}) \quad (1)$$

where $\dot{Q}_{amb}$ are theambient losses, $E_r$is the eventual measurement error, $\dot{M}_{sf}$ is the mass flow rate of secondary fluid of the heat exchanger $C_{p,sf}$ is the specific heat capacity of the secondary fluid, $T_{sf1}$and T_{sf2} are the inlet and outlet temperature of the secondary fluid in the heat exchanger, $\dot{M}_{wf}$ is the working fluid mass flowrate and $h_{wf,1} and\ h_{wf,2}$ are the inlet and outlet specific enthalpy of working fluid.

2.5.2 Pump efficiency

The pump power consumption was not measured during the test campaign. For the needs of the comparison, the pump efficiency was supposed constant and equal to 50%. This isentropic efficiency would be calculated as follows:

$$\epsilon_{s,pp} = \frac{\dot{W}_s}{\dot{W}} = \frac{\dot{M}_{wf}\left(h_{wf,ex,pp,s} - h_{wf,su,pp}\right)}{\dot{W}_{el}} \quad (3)$$

2.5.2 Expansion machine efficiency

In a first approach, the isentropic efficiency of the turbine is used to characterize the performance of the component. It is calculated as follows:

$$\epsilon_{s,exp} = \frac{\dot{W}}{\dot{W}_s} = \frac{\dot{W}_{el}}{\dot{M}_{wf}\left(h_{wf,su\_exp} - h_{wf,ex,exp,s}\right)} \quad (4)$$

3 Results and discussion

As explained, the heat balances over the heat exchangers are calculated in order to ensure the consistency of the measured data. As it can be seen on figure 4(a) and (b), the balances are good. Both exchangers being insulated, the difference between the heat flow rate on the secondary fluid side and the one on the working fluid side is practically null. The maximal difference is around 3% for the highest temperature levels for which the uncertainty of the type-t thermocouples is slightly increased.

The energy conservation was then also verified for the rotating machines

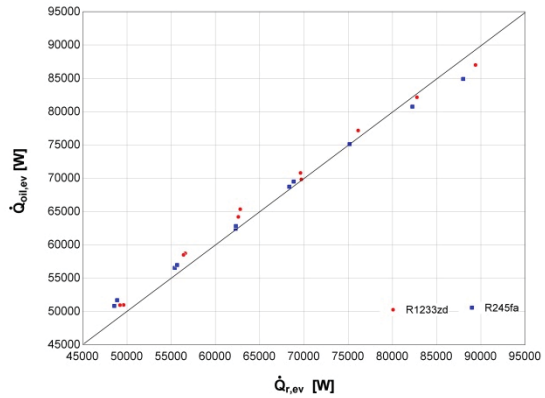

Figure 4(a): *Heat balance over the evaporator for both R245fa and R1233zd*

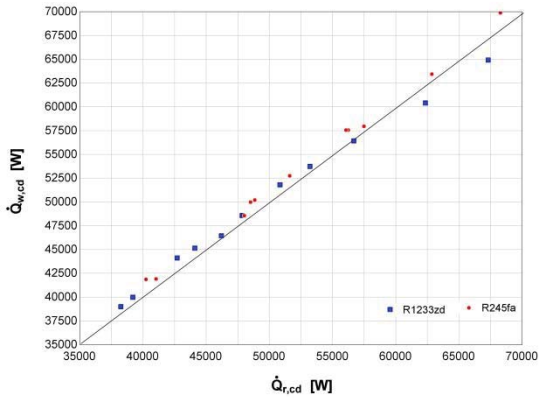

Figure 4(b): *Heat balance over the condenser for both R245fa and R1233zd*

The energy conservation being respected for all the components of the rig, the measurements appearing coherent, the investigated comparison could be started.

As explained, the comparison of the two fluids was realized in the particular case study of WHRORC for truck application. For these applications, the main constraint is generally the condensing temperature because of the high temperature of the possible inboard heat sink. A fluid whose condensing pressure level is lower for the same saturation temperature will be preferred.

On the other hand, the evaporating pressure is generally an optimization variable of the WHR system. It is optimized to maximise the power output of the ORC.

Therefore it was decided to compare both fluids for the same condensing temperature and the same evaporating pressure (Figure 5).

Results are then compared in terms of

- working fluid mass flow rate
- pump power consumption: assuming a constant isentropic efficiency
- turbine power production

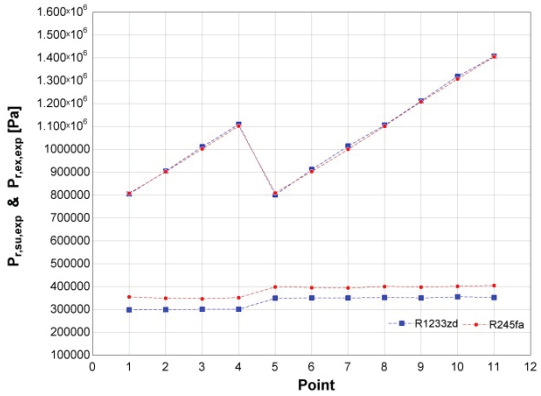

Figure 5(a): *Evaporating and condensing pressure levels for both R245fa and R1233zd*

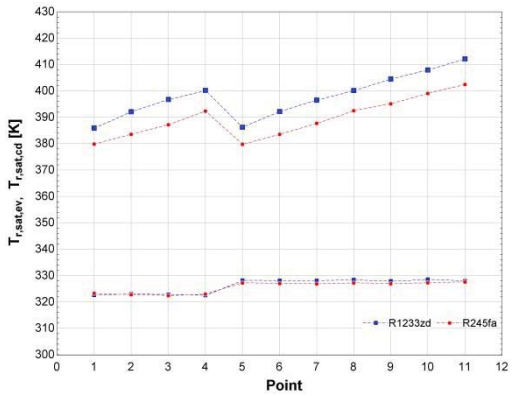

Figure 5(b): *Evaporating and condensing temperature levels for both R245fa and R1233zd*

Regarding mass flow, it can be observed that achieving the conditions of pressure of this comparison leads to the same mass flow rates for both fluids. Indeed, both fluids are practically identical regarding densities. The turbine imposing the flow rate for an inlet pressure, the evaporating pressures being the same, mass flow rates are also the same (Figure 6(a)).

Nonetheless, assuming a constant for the pump in each case, the pump power consumption would be slightly lower in case of R1233zd (Figure 6(b)).

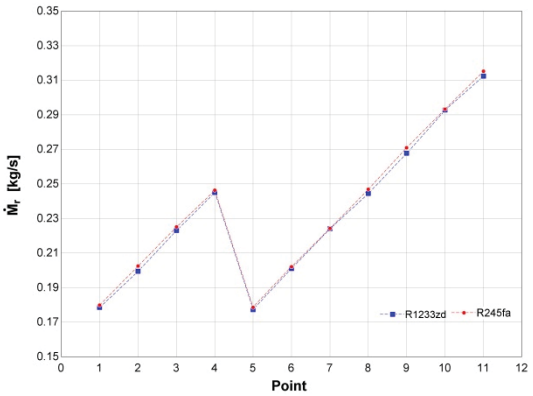

Figure 6(a): *Mass flow rate of working fluid both R245fa and R1233zd*

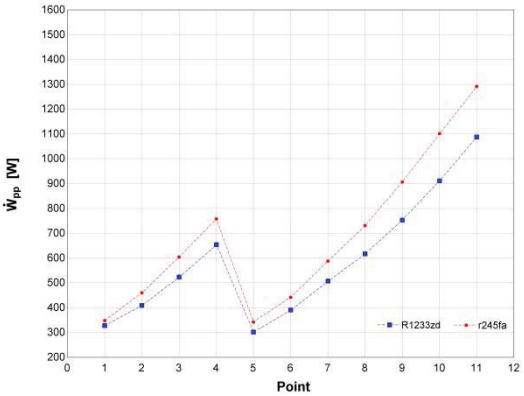

Figure 6(b): *Pump power consumption both R245fa and R1233zd*

Finally, the power produced by the turbine is compared for both fluids. For confidentiality reasons, but to give order of magnitudes:

- It is first compared from a hypothetical aspect (Figure 7(a)) assuming, as for the pump, a constant isentropic efficiency (60%).
- The real active powers produced during the experiment are then made dimensionless and compared (Figure 7(b)).

As it could be expected, the power produced is always higher using R1233zd. Because of the comparison method, the pressure ratio over the turbine is in each case higher than for R245fa. Since the mass flow rates are the same, the fluids begin very similar, the power produced is increased when using R1233zd.

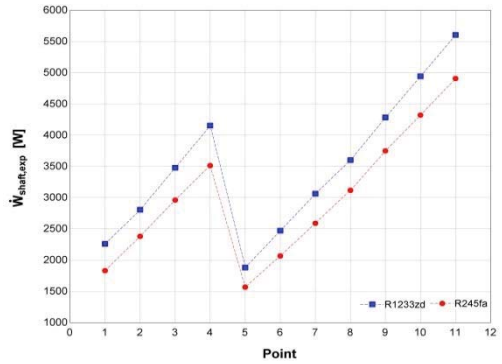

Figure 7(a): *Theoretical power produced by the expansion machine assuming a constant isentropic efficiency of 60 % both R245fa and R1233zd*

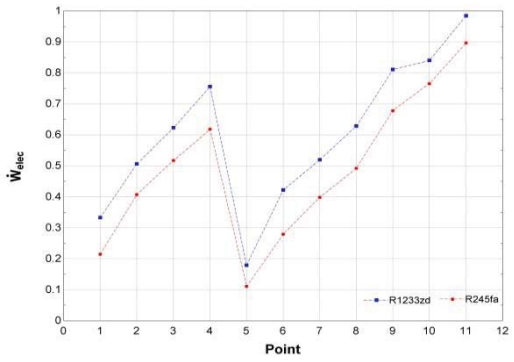

Figure 7(b): *Experimental power produced by the turbine both R245fa and R1233zd*

4 Conclusions

The objective of this study was to compare the performance of an ORC system using a radial turbine and exploiting the waste heat out of a truck for two working fluids: R245fa and R1233zd.

A test rig integrating the turbine was built and several measurements points were realized for both fluids. Some of these points were then used to compare the performance of the ORC components for same condensing temperature and same evaporating pressures. This method was identified as appropriate considering the particular case of waste heat recovery for truck applications. Indeed, the constraint for the ORC, in this case, is generally the condensing temperature because of the mid-to-high temperature heat sinks only available onboard. A fluid with a lower condensing pressure for a same saturation temperature level is therefore suited. On the other hand, the evaporating pressure is generally optimized for these ORC systems. So there was no point to compare the same evaporating temperature levels

Results were then compared in terms of working fluid mass flow rate, pump consumption and turbine production. It was shown that the temperature and pressure conditions used for the comparison led to the same mass flow rates for both fluids. Nonetheless, the pump consumption was slightly lower in case of R1233zd. The power produced by the turbine was always higher when using R1233zd because of the higher pressure ratio resulting of the comparison method.

Acknowledgement

The results presented in this paper have been obtained within the frame of the NoWaste project funded by the European Commission. This financial support is gratefully acknowledged.

References

[1] European Commission. Energy 2020. http://ec.europa.eu/energy/energy2020/energy2020en:htm; 2013

[2] European Commission. Towards a strategy to address co2 emissions from hdv. http://ec.europa.eu/clima/policies/transport/vehicles/heavy/indexen:htm; 2013

[3] IEA. 2014 key world energy statistics. http://www.iea.org/publications/freepublications//publication/KeyWorld2014.pdf, 2014.

[4] J. Bao, L. Zhao. A review of working fluid and expander selections for organic rankine cycle. Renewable and Sustainable Energy Reviews, 2013.

[5] P. Kokic. A probabilistic analysis of human influence on recent record global mean temperature changes. Climate Risk Management, 3, 2014.

[6] S. Quoilin, M. Van Den Broek, S.Declaye, P. Dewallef, V. Lemort. Techno-economic survey of organic rankine cycle (orc) systems. Renewable and Sustainable Energy Reviews, 2013.

[7] UNFCCC. Kyoto protocol to the united nations framework convention on climate change. http://unfccc.int/resource/docs/convkp/kpeng.html, 1992.

Compact LP/MILP Models for Decentralized Co-generation Plant Optimization

Michael Short [a*], Muneeb Dawood [a], Tracey Crosbie [a] and Nashwan Dawood [a]

[a] Technology Futures Institute, Teesside University, Middlesbrough, TS1 3BA, UK
* Corresponding author. Email: m.short@tees.ac.uk

Abstract
Environmental concerns combined with the liberalization of the energy markets has forced a rethink in the way that energy is generated and distributed, leading to the emergence of small to medium-scale decentralised generation equipment embedded within the transmission and distribution networks. In this paper the focus is upon unit commitment scheduling and economic dispatch optimization for a small/medium scale decentralized CHP plant. The plant is assumed to be equipped with local heat and electricity storage and operating in the presence fluctuating wholesale energy prices and local loads. A compact linear optimization model is described to efficiently model the optimization and scheduling problem over a short planning horizon. The optimization is intended to be repeated hourly in a receding horizon fashion.

Keywords: decentralised CHP plant; vonvex optimization; mixed integer linear programming.

1 Introduction

The liberalization of the energy markets in combination with environmental concerns has forced a rethink in the way that energy is now generated and distributed to consumers [1, 2]. In particular, the emergence of small- and medium-scale generation equipment (typically driven by renewable or alternative forms of energy conversion) embedded within the transmission and distribution networks is becoming increasingly commonplace. This paper is concerned with the repetitive cost-optimal balancing of hourly supply and demand for heat and electricity using a small/medium-scale decentralized Combined Heat and Power (CHP) cogeneration plant equipped with both heat and electricity storage. Cogeneration systems are broadly defined as the coincident generation of multiple forms of energy from a single fuel source: for CHP, the energy produced is the combined production of electric power and useable heat [3]. Cogeneration using CHP is an increasingly important component of energy production technology in Europe and other continents [3, 4]. Here we assume the plant is serving a local load (heat and electricity) and operating in the presence of a wholesale energy market with fluctuating energy prices. The economic dispatch problem is, given a series of future hourly electrical and heat loads along with prices for buying/selling electricity and heat wholesale, determine an plan for the hourly settings for CHP production, energy storage/retrieval and wholesale energy buying/selling that minimizes the expected economic costs and respects natural system constraints [4]. Clearly, load information is not known accurately and the optimizer must employ predictions for these unknown quantities, and must be reactive when the state of the system evolves and more reliable or accurate information is revealed or acquired [4, 5, 6, 7]. For this reason the optimization problem must be efficient enough to allow regular re-solution. This paper describes simple but accurate mathematical models that capture the salient techno-economic characteristics of the economic dispatch problem in the form of a Linear Program (LP). The model may be used with optional binary variables representing hourly on/off states of the plant to solve the related unit commitment scheduling problem as a Mixed Integer LP (MILP). The remainder of this paper is organized as follows. Section 2 presents an overview of the rolling horizon optimization concept. Section 3 presents the optimization models. A short conclusion can be found in Section 4.

2 Rolling Horizon Optimization Concept

The emergence of generation equipment embedded within energy transmission and distribution networks has helped to push forward the concept of the smart grid: an energy distribution network that not only allows for the physical transfer of energy but also features heavy automation and ICT support [2]. This ICT infrastructure offers many opportunities for improved monitoring, control and optimization. One such improvement is the optimal economic balancing of energy supply with demand. Since predictions of unknown quantities such as future demand must be employed, any optimization

must be reactive to system state changes and information updates. As such, the concepts of adaptive control (to track and adapt to changing environment conditions and supply/demand trends) [8] and receding-horizon predictive control (to re-calculate cost-optimal corrective strategies) [9] can be employed. Henceforth, we assume that time is indexed by the non-negative integer t which counts the number of elapsed hours since system switch-on. At hour t, a dispatch optimization problem and (optionally) a related unit commitment problem are to be solved, considering a planning horizon of H hours. In other words, the decisions which are possible for each hour in the range $[t, t+H)$ are optimized using the knowledge available at time t. The optimal decisions for the hour t are then applied. At time $t+1$, the optimization is then repeated for the time range $[t+1, t+H+1)$ using the knowledge available at time $t+1$, and this process repeats indefinitely. Equipment costs for purchasing and installing equipment such as the CHP plant itself are considered as sunk costs which cannot be optimized. We assume that heat and electricity load forecasting methods appropriate for a small/medium scale CHP plant (see, e.g. [6]) are carried out prior to each optimization. Descriptions of a suitable PC-based ICT infrastructure to support the required data acquisition, prediction and optimization may be found in related work by the authors [7].

3 Compact linear models

3.1 CHP plant

A CHP plant is normally one of two distinct types of construction: a backpressure unit or extraction-type unit [4][5][10][11]. The former typically has a fixed ratio β of rate of heat transfer (ΔQ) to electrical power (P) production, and operates by reclaiming heat from the steam exiting the turbine. The heat/power ratio β is approximately constant over the majority of its working operating range. The latter, however, allows some independence in the levels of heat and electricity generated by allowing a varying level of high-pressure steam extraction. This gives a variable heat/power ratio which is adjustable over a prescribed operating range. For the large majority of CHP units the allowed operating region is a convex polytope, and this can be captured in a model using inequalities connecting its extreme points [4][10]. In this paper we assume that β is adjustable on an hourly basis, and for the hour ending at time t, $\beta(t)$ denotes the employed ratio which is assumed to satisfy the common relationship $\beta_{\text{Min}} \leq \beta(t) \leq \beta_{\text{Max}}$ [10]. Let $P(t)$ and $\Delta Q(t)$ be the electrical power output and rate of heat transfer during hour t respectively, and the constant PQ_{Max} represent the maximum output of the plant at full boiler load. Then the inequalities $P(t)\beta_{\text{Min}} \leq \Delta Q(t) \leq P(t)\beta_{\text{Max}}$, $P(t) + \Delta Q(t) \leq PQ_{\text{Max}}$ in addition to $\Delta Q(t) \geq 0$ and $P(t) \geq 0$ are sufficient to describe the convex region. For a backpressure unit with fixed β, we may simply set $\beta_{\text{Min}} = \beta_{\text{Max}} = \beta$. A variety of models including linear, mixed-integer linear and non-linear have been developed to model the economic costs for short-term optimization of CHP plant [4][5]. Although non-linear and mixed-integer models give more accurate results, extensive investigation has found that the optimality gap between the two is very small, typically ≤ 3% in representative cases [5]. Linear models – whilst producing slightly different solutions to a non-linear model – are much more computationally efficient and less sensitive to input parameter changes [5]. Since both of these properties are desired for short-term optimization [10][11], a linear model is adopted in this work. The loss of accuracy is quite small and mainly occurs due to efficiency losses in the low-load region of boiler operation, typically < 30% full load. A low demand to induce this level of loading occurs quite infrequently, especially during winter months, if the plant has been correctly sized. The relationship between boiler load L (%) and efficiency $\eta(L)$ (%) is well modelled by a quadratic equation of the form $\eta(L) = A + B\,L + C\,L^2$ for suitable constants A, B, and C [5][11]. A typical efficiency curve for a medium-scale CHP plant (reproduced from [5]) is shown in Figure 1 (left). The relationship is concave, increasing to a maximum efficiency of typically 90% – 95%. From Figure 1 (right), one sees that this produces a sigmoidal relationship between the required input fuelling rate F (and hence the hourly fuel cost C) and the load L, shown as a % age of the maximum available. The upper part of the relationship is convex, and since fuelling is a cost to be minimized may be approximated by piecewise affine functions. The lower part of the relationship (for loads less than ≈ 30%) is concave and cannot be approximated in such a fashion.

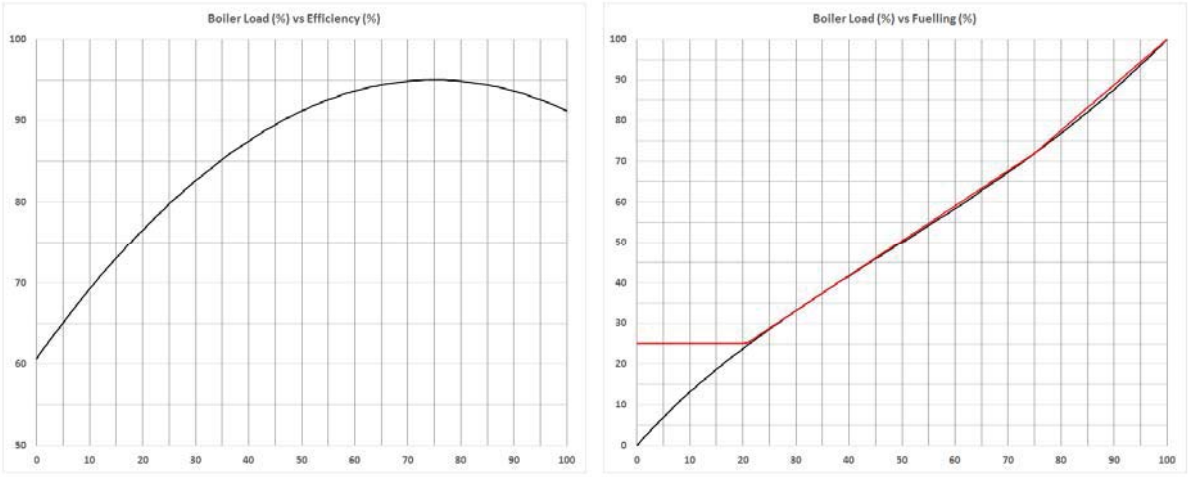

Figure 1: *(Left): Boiler efficiency as a function of load, (Right): required fuelling as a function of boiler load in black, with piecewise approximation in red*

Thus the relationship is usually modelled as a single linear function of the form $F = \eta_{Max} L$, with η_{Max} being the efficiency of the boiler at full load [5]. With such a model, the plant is then assumed to be operable efficiently at very low load, which is not the case; minimum load constraints can be employed to enforce operation in the efficient boiler regions, but the CHP plant is then forced to operate continuously in the model regardless of the need for heat or power. Both assumptions lead to inaccuracies [5]. In reality, there are numerous operational and legislative reasons why CHP boiler units are constrained to operate with some minimum fuelling or loading constraints. This can be for operational and safety reasons, such as the need to maintain combustion of the fuel bed and ensure adequate circulation of steam and water in the boiler drum [5][12]. Most boilers have an operational lower load of ≈ 20% - 30% full load [5]. There are also legislative constraints, such as the need to maintain flue gas temperatures at minimum levels to comply with emissions regulations, and fiscal incentives often require demonstration that a threshold boiler efficiency level (typically 70%) is achieved as a precursor to acquiring a 'CHP quality index' [13]. For a modern CHP plant with co-ordinated control system for the boiler, turbine and heat exchanger, operation at low output power levels is nevertheless achievable with a steam bypass valve [12]. The co-ordinated control system can use such a valve to allow some of the generated steam to bypass the turbine/extractor and divert straight to the condenser such that at very low output levels, the boiler fuelling is held at the minimum required level. Therefore we propose to approximate the fuelling costs with three affine functions of the form $f_i(x) = a_i + b_i x$, $i = 1, 2, 3$, such that $b_3 \geq b_2 \geq b_1$ to ensure convexity. The first function has a slope of zero and enforces a minimum fuelling and boiler loading. The second is drawn from the point of maximum efficiency tangential to the lower part of the cost curve, while the third connects the point of maximum efficiency with the point of full load. The fuelling function may then be taken as $F(L) = min\{f_1(L), f_2(L), f_3(L)\}$ which is easily modelled in the LP by substituting $L = P(t) + \Delta Q(t)$, and using a slack variable z_1 plus three inequalities of the form $z_1 \geq f_i(P(t) + \Delta Q(t))$, $i = 1, 2, 3$. For the cost curve shown in Figure 1 (right), the resulting approximation using a minimum fuelling constraint of 25% (to ensure boiler load > 20% and efficiency > 75%) is obtained with $\{a_i, b_i\}$ values as: {25.00, 0.000}, {7.200, 0.865} and {1.120, -12.000}. The piecewise approximation has an error < 1.2 % over the working range of the boiler. Defining the unit fuelling cost as C_F, then the term $z_1 C_F$ is incorporated into the cost function to represent the economic costs.

Since operation at low and zero output levels can be modelled thus, but it is relatively inefficient to do so (in both the model and in reality), it is also beneficial to be able to shut down the plant when it is economically justified. In the optimization model this allows the 'unit commitment' scheduling problem to be integrated with the CHP economic dispatch problem. To facilitate such operations we introduce hourly binary indicator variables $I(t) \in [0, 1]$ with the interpretation that for $I(t)$ = '1', the plant is switched on for hour t and for $I(t)$ = '0' the plant is switched off. By modifying the constraint $P(t) + \Delta Q(t) \leq PQ_{\text{Max}}$ to the form $P(t) + \Delta Q(t) \leq I(t)\, PQ_{\text{Max}}$, both the electrical power and rate of heat transfer

are forced to zero when $I(t) = 0$. The latter is ensured as when $I(t) = 0$, the condition $P(t) + \Delta Q(t) \leq 0$ must hold with both terms also being non-negative. In terms of operating costs, let the savings that occur when the plant switched off be denoted as C_{Off}, and let the minimum fuelling costs be denoted as $C_{Fmin} = C(0)$. Then adding the terms $I(t)\ C_{Off}$ - (1- $I(t)$) C_{Fmin} into the cost function ensures that when $I(t)$ = '0' the operating cost is driven to zero, and when $I(t)$ = '1' the cost is equal to C_{Off} plus that incurred for the fuel used. If costs of C_{SS} are incurred every time the plant is shutdown or started up, then this is modelled by using the slack variable z_2 and adding the constraints $z_2 \geq (I(t) - I(t\text{-}1))$ and $z_2 \geq -(I(t) - I(t\text{-}1))$. This ensures that when $I(t) \neq I(t\text{-}1)$, z_2 is forced to '1' and zero otherwise; the term $z_2\ C_{SS}$ is then incorporated into the cost function. The final aspects to be considered are those related to hourly constraints on the rate at which the combined power output of the plant can be changed. Assuming that the rate limits are ΔP_{Max} and ΔP_{Min}, constraints of the form $\Delta P_{Min} \leq (P(t) + \Delta Q(t)) - (P(t\text{-}1) + \Delta Q(t\text{-}1)) \leq \Delta P_{Max}$ are used. The overall model for each hour of CHP plant operation is summarized below. The efficiencies of the turbine / generator and heat exchanger (η_E and η_H respectively) are not explicitly included, and should be added as factors in additional constraints related to energy balances. Before such constraints are considered, models for energy storage are discussed in the next Section. Note that if unit commitment scheduling is not required, the $I(t)$ variables can be set to '1' and eliminated from the representation to leave a basic LP.

Costs:	$z_1(t)\ C_F + z_2(t)\ C_{SS} + I(t)\ (C_{Off} + C_{Fmin}) - C_{Fmin}$;
Decision Variables:	$P(t)$, $\Delta Q(t)$, $I(t)$;
Slack Variables:	$z_1(t)$, $z_2(t)$;
Constraints:	$P(t) \geq 0$, $\Delta Q(t) \geq 0$, $z_1 \geq 0$, $z_2 \geq 0$, $I(t) \in [0, 1]$ and integer;
	$z_1(t) \geq a_i + b_i\ (P(t) + \Delta Q(t))$, $i = 1, 2, 3$;
	$P(t) + \Delta Q(t) \leq I(t)\ PQ_{\text{Max}}$;
	$P(t)\beta_{\text{Min}} \leq \Delta Q(t) \leq P(t)\beta_{\text{Max}}$;
	$z_2(t) \geq (I(t) - I(t\text{-}1))$, $z_2(t) \geq -(I(t) - I(t\text{-}1))$;
	$\Delta P_{Min} \leq (P(t) + \Delta Q(t)) - (P(t\text{-}1) + \Delta Q(t\text{-}1)) \leq \Delta P_{Max}$;

3.1 Linear storage and additional model elements

Let the energy stored in the heat accumulator at hour t be denoted as $C_H(t)$, and the equivalent amount of electrical energy stored at hour t be denoted as $C_E(t)$. Let the energy stored/extracted to/from the heat accumulator at hour t be denoted as $\Delta C_H(t)$, and the equivalent amount of electrical energy stored/extracted to/from the store at hour t be denoted as $\Delta C_E(t)$. We assume that (1) there is an energy storage loss associated with each store, and (2) a capacitive loss of energy associated with each store over time. We assume that the limits of storage are constrained to be $0 \leq C_H(t) \leq C_{HMax}$ and $0 \leq C_E(t) \leq C_{EMax}$, and the limits of rate-of-change of storage are constrained to be $\Delta C_{HMin} \leq \Delta C_H(t) \leq \Delta C_{HMax}$ and $\Delta C_{EMin} \leq \Delta C_{EMax} \leq \Delta C_{EMax}$. An auto regressive model with controlled input is assumed to describe the evolution of the energy content of each of the storage facilities at hour t, such that $C_H(t) = C_{H\alpha}\, C_H(t\text{-}1) + C_{H\beta}\, \Delta C_H(t)$ and $C_E(t) = C_{E\alpha}\, C_E(t\text{-}1) + C_{E\beta}\, \Delta C_E(t)$. The parameters $C_{H\alpha} \in (0, 1]$ and $C_{E\alpha} \in (0, 1]$ represent the capacitive loss factors of the store and $C_{H\beta} \in (0, 1]$ and $C_{E\beta} \in (0, 1]$ represent the energy conversion loss factors of the store; a proportion of energy is assumed lost during both storage and retrieval. The overall model for each hour of operation is summarized as below:

Decision Variables:	$\Delta C_H(t)$, $\Delta C_E(t)$;
Slack Variables:	$C_H(t)$, $C_E(t)$;
Constraints:	$C_H(t) = C_{H\alpha}\, C_H(t\text{-}1) + C_{H\beta}\, \Delta C_H(t)$, $C_E(t) = C_{E\alpha}\, C_E(t\text{-}1) + C_{E\beta}\, \Delta C_E(t)$;
	$0 \leq C_H(t) \leq C_{HMax}$, $0 \leq C_E(t) \leq C_{EMax}$;
	$\Delta C_{HMin} \leq \Delta C_H(t) \leq \Delta C_{HMax}$, $\Delta C_{EMin} \leq \Delta C_{EMax} \leq \Delta C_{EMax}$;

Let the predicted demands for heat and electricity during hour t be denoted as $D_H(t)$ and $D_E(t)$, and the associated prices for buying/selling heat and electricity during hour t be denoted as $C_{HB}(t)$, $C_{HS}(t)$, $C_{EB}(t)$ and $C_{HS}(t)$ respectively. Let the amount of heat and electricity that is to be bought/sold by the plant operator during hour t be denoted as $X_{HB}(t)$, $X_{HS}(t)$, $X_{EB}(t)$ and $X_{HS}(t)$. Then for each hour t the following

additional costs and constraints are employed in the optimization to ensure that both electrical and heat supply and demand are balanced:

Costs: $C_{HS}(t)\,X_{HS}(t) + C_{ES}(t)\,X_{ES}(t) - C_{HB}(t)\,X_{HB}(t) + C_{EB}(t)\,X_{EB}(t)$;

Decision Variables: $X_{HB}(t)$, $X_{HS}(t)$, $X_{EB}(t)$, $X_{HS}(t)$;

Constraints: $X_{HB}(t) > 0$, $X_{HS}(t) > 0$, $X_{EB}(t) > 0$, $X_{HS}(t) > 0$;

$\Delta Q(t)\,\eta_H + X_{HB}(t) - X_{HS}(t) - \Delta C_H(t) = D_H(t)$;

$P(t)\,\eta_E + X_{EB}(t) - X_{ES}(t) - \Delta C_E(t) = D_E(t)$;

4 Conclusions

This paper has described a compact linear optimization model to capture the salient techno-economic characteristics of the economic dispatch problem for a decentralized CHP plant in the form of a LP. Optional binary variables are introduced to the model allowing the solution of the related unit commitment scheduling problem as a MILP. Our initial tests of the model indicate that it is both efficient and accurate. Future work will concentrate upon more extensive numerical evaluations of accuracy and computation time when applied to a real case study.

Acknowledgement

This research described in this paper was carried out in the context of the IDEAS Collaborative Project (Grant Agreement No. 600071) which is co-funded by the European Commission, Information Society and Media Directorate General, under the Seventh Framework Programme (FP7), Cooperation theme three, “Information and Communication Technologies”.

References

[1] G. Masters, *Renewable and Efficient Electric Power Systems*. New Jersey: John Wiley & Sons, 2004.

[2] J. Ekanayake, N. Jenkins, K. Liyanage, J. Wu & A. Yokoyama, *Smart Grid: Technology and Applications*, Wiley-Blackwell, 2012.

[3] N. Petchers, *Combined Heating, Cooling & Power Handbook: Technologies & Applications: An Integrated Approach To Energy Resource Optimization*, The Fairmont Press, 2003.

[4] F. Salgado & P. Pedrero, Short-term operation planning on cogeneration systems: A survey, *Electric Power Systems Research*, Vol. 78, pp. 835–848, 2008.

[5] T. Ommen, W.B. Markussen & B. Elmegaard, Comparison of linear, mixed integer and non-linear programming methods in energy system dispatch modelling, *Energy*, Vol. 74, pp. 109-118, 2014.

[6] M. Short, M. Dawood, T. Crosbie, N. Dawood, Adaptive Load Forecasting for Decentralized Co-generation Plant, To be presented at SusTEM 2015, Newcastle, UK, July 2015.

[7] M. Short, M. Dawood, U. Shvadron, J. Ye, D. Gras & M. Ala-Juusela. *Specifications for a neighbourhood energy management tool*, Deliverable D3.2 of the IDEAS project, November 2013. Available at http://www.ideasproject.eu.

[8] K.J. Astrom & B. Wittenmark, *Adaptive Control: 2nd Edition*, Addison-Wesley, 1995.

[9] E.F. Camacho & C. Bordons, *Model Predictive Control* (*2nd Edition*), Springer Verlag, 2004.

[10] R. Lahdelma & H. Hakonen, An efficient linear programming algorithm for combined heat and power production, *European Journal of Operational Research*, Vol. 148, pp. 141-151, 2003.

[11] E. Thorin, H. Brand & C. Weber, Summary of specified general model for CHP system, *OSCOGEN EU FP5 Project Deliverable D4.1*, April 2001.

[12] A. Ordys, A.W. Pike, M.A. Johnson, R. M. Katebi & M.J. Grimble, *Advances in Industrial Control: Modelling and Simulation of Power Generation Plants*, Springer-Verlag London Ltd, 1994.

[13] Department of Energy and Climate Change (DECC), *Quality Assurance for Combined Heat and Power: Issue 5*, November 2013.

Evaluation of Practical Applications of Integrated Exhaust Energy Recovery (EER) on Vehicles

Zhijun Peng*[a], George Haritos [a], Tianyou Wang [b], Yajun Zhang [b]

[a] School of Engineering and Technology, University of Hertfordshire, UK
[b] Stake Key Laboratory of Engine, Tianjin University, China
* Corresponding author: z.peng2@herts.ac.uk

Abstract

In the study presented in this paper, an analytic model was built for examining the environmental and economic benefits of integrated EER systems. Then the improvement on the total powertrain efficiency and net reduction of CO_2 emissions were investigated, in terms of the average vehicle used in the UK. Results show that, for light duty vehicles fitted with thermal cycle EER system, the cost increase could be paid back in 10.1 years and CO_2 emission could be paid back in just 1.9 years, compared to Hybrid Electric Vehicle's (HEV's) 11.9 years and 1.4 years for cost and CO_2 emission, respectively. When the annual fuel price increase is considered, the cost pay-back is reduced to 8.1 years for EER vehicles and 8.9 years for HEVs. Higher mileage vehicles will have more obvious advantage for fitting EER system. When doubled annual mileage is considered, EER system can reduce the cost and CO_2 emission pay-back times to 2.7 years and 0.6 years, compared to HEV's 8.5 and 2.7 years, respectively.

1 Introduction

When the cost for obtaining the engine combustion efficiency improvement is becoming significantly high, technology innovation around vehicle powertrain has involved more on hybrid configuration (such as Hybrid Electric Vehicles - HEVs) and integrated Exhaust Energy Recovery (EER) in recent years. In the current research, integrated EER refers to those new technologies beyond conventional uses for exhaust waste heat such as turbocharger or cabin air-heating. While HEV technology has achieved considerable market share in recent years, R&D on EER is being paid more attention, particularly while energy collected by EER can be easily applied on HEVs [1, 2, 3].

Normally the maximum net brake efficiency of Internal Combustion (IC) engines is difficult to be higher than 42% [4], large amount fuel energy is rejected from the engine to the surroundings as waste heat in several forms, with a significant fraction through the exhaust. A recent study [5] estimated in a typical 2.0 litre gasoline engine used on passenger cars, 21% of the released energy is wasted through the exhaust at the most common load and speed range. The fraction increases to 44% at the peak power point. On average, about one third of energy generated from the fuel is wasted via exhaust gases. Current estimates of waste thermal energy from ground vehicle systems range from 20kW to 400 kW, depending on engine size and engine torque-speed conditions. This is equivalent to annually 45 billion gallons of gasoline fuel lost through the exhaust pipes of the 240 million light-duty passenger (LDP) vehicles in USA alone [6].

LDP vehicle exhaust systems operate at gas temperatures from 500 to 900 °C, typically between 600 and 700 °C. For Heavy-Duty (HD) vehicles, exhaust gas temperatures range from 500 to 650 °C under general driving condition. These can be further boosted during periodical regenerations of diesel particulate filter (DPF) and other aftertreatment advices [7]. Those high exhaust temperatures provide significant opportunities for EER to generate energy for increasing powertrain's efficiency [6, 8].

Integrated EER which has been mainly focused in recent years mainly include thermal cycle system based on Rankine Cycle (RC) and Thermoelectric (TE) regeneration. The latter can directly convert part of the exhaust heat to electric power through the thermoelectric phenomenon, without the use of mechanically rotating parts, and providing some advantages such as compact package, without noise and vibration, and high reliability. However, there exist significant system design challenges during the development of TE system due to its low conversion efficiency and relatively high costs of thermoelectric semiconductor materials [9, 10].

The conversion of exhaust heat energy into useful power by integrated EER system would not just bring measurable advantages for improving fuel consumption but also increase engine power output (power density) or vehicle downsizing, further reducing CO_2 and other harmful exhaust emissions correspondingly. When the benefit on fuel cost and emission reductions provided by EER have been approached more or less, its economic benefit has not been depicted clearly. For promoting the development of EER systems and its commercialization, it is necessary to provide necessary information about its pay-back times of both cost and carbon emissions. In this paper, average EER efficiency based on New European Driving Cycle (NEDC) would be estimated by investigating recoverable exhaust sensible heat of a light duty gasoline powertrain. Then the environmental and economic benefits of EER vehicles will be analysed by considering average driving condition in the UK.

2 Analysis of cost and CO_2 emissions of EER vehicles

Based on previous study on a passenger car engine, it suggests the net EER efficiency can be around 20% for the powertrain [2]. This figure will be used for the following section for estimating the cost and carbon emissions of EER vehicles (vehicles fitted with EER system) and their pay-back times of cost and carbon emissions, though it is understood that there is some difference for the efficiency for different vehicles regarding their powertrain configurations and operating conditions.

In the following sections, in addition to compare EER vehicles (vehicles fitted with EER system) with pure Internal Combustion Engine (ICE) vehicles, Hybrid Electric Vehicles (HEVs) and HEV+EER vehicles are also considered, while EER system can be electrically connected with HEV for its work output. Powertrain system setup of two configurations of HEV and HEV+EER can be used as shown in Figure 1.

In Figure 1, the power contribution from different energy sources are represented as the shape size. For example, from HEV to HEV+EER, the engine can get further downsizing. Then the engine size and fuel tank size become smaller and the battery size of HEV+EER gets bigger.

In Figure 2, it shows total cost variations with used years for ICE vehicles, EER vehicles, HEVs and HEV+EER vehicles. Those results are achieved from an analysis based on vehicles sold and used in the UK where the average new passenger car price is approximately £27500 in 2011. For HEV, 20% higher average price is added by considering the actual cost of HEVs in the current market. Those data come from DivenData whose published data can be found at www.drivendata.co.uk. For EER vehicles, the cost increase of 10% is estimated by including costs of all mechanical hardware (evaporator, expander, condenser, pump and gearbox) and control system. For HEV+EER vehicles, only 25% average cost increase rather than 30% (20% for HEV and 10% for EER) is added since the electrical work output of EER system could be easily implemented compared to EER mechanical work output configuration.

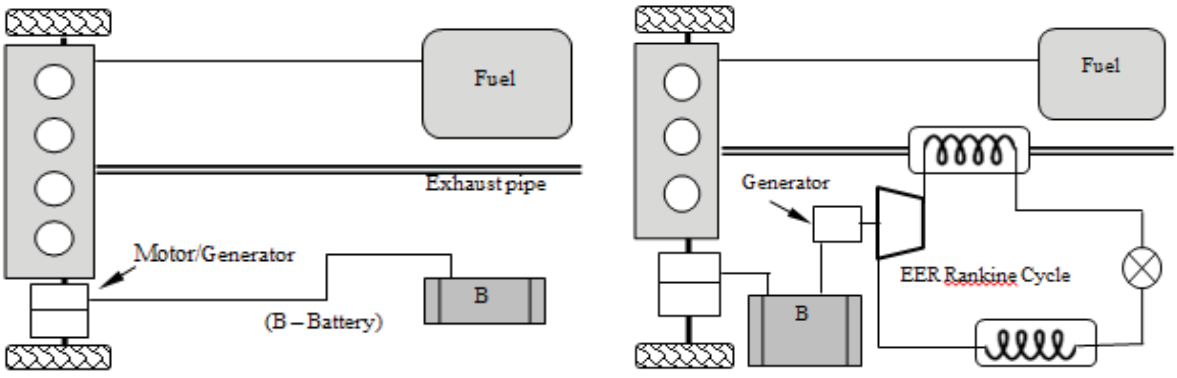

(a) (b)

Figure 1: (a) *General HEV system layout;* (b) *EER system with electrical power output to HEV*

The annual average cost of vehicles is calculated by including fuel, service, annual authority inspection (in the UK this is named as MOT – Ministry of Transport), insurance and tax. For vehicles used in the UK, the fuel cost is based on the average annual mileage of 12000 miles for the first year new cars, 10000 miles the second year and 8000 miles per year for the following years [11]. ICE vehicles' average fuel consumption is currently about 0.09 litre/mile, compared to 40% of HEV's saving which was reported by NREL (National Renewable Energy Laboratory) [12] and Ting et al. [13]. From the study in the last section, EER's 20% saving on fuel consumption is selected. Combining HEV's and EER's individual savings, 50% saving is assumed for HEV+EER in the present analysis. With regard to the average fuel cost, the current price £1.40/litre in the UK market is used for the calculation. For other annual costs, tax exemption but increased service cost for HEV vehicles are considered.

Then cumulative CO_2 emissions and cumulative cost can be formulated as:

$$CO_{2-cumulative} = CO_{2-embedded} + S_{cumulative} \times FC \times \rho_{fuel} \times x_c \times 44/12 \quad (4)$$

Where $S_{cumulative}$ is the cumulative mileage. FC is the fuel consumption (litre/mile). ρ_{fuel} is fuel density (kg/litre). x_c is carbon content rate of fuel. 44 and 12 are the molecular weight of carbon dioxide and that of carbon, respectively.

$$Cost_{cumulative} = Cost_{embedded} + S_{cumulative} \times FC \times P_{fuel} + \sum_{0}^{n}(Ins + Tax + MOT + Service) \quad (5)$$

Where P_{fuel} is fuel price (pound/litre) and *Ins* represents annual insurance cost, respectively.

In Figure 2 it can be found that with fixed fuel price, the saving on fuel cost from HEV vehicles could not pay back the cost increase in 10 years due to the high purchase cost. With further estimate, the cost pay-back time for HEV vehicles is about 11.9 years. For EER vehicles, it roughly needs 10.0 years for paying back the cost increase. It suggests EER vehicle would probably be a more attractive option than HEV vehicle for customers, if their concerns are more on the vehicle and operating costs, rather than the fuel saving or carbon emission reduction. When customers make an estimate for the total vehicle cost (purchase cost and operating cost), the current fuel price is always cited since the future of fuel price is always difficult to predict. Therefore, from the analysis shown in Figure 2, it can be assumed that EER vehicles could be promoted for the purpose of fuel or carbon emission saving, at least compared to HEV vehicles. As EER vehicles may be more popular than HEV vehicles, their possible high market share would be helpful to get more CO_2 emission reduction, although EER vehicles' fuel saving rate is lower than HEV vehicles.

The estimated pay-back times of various vehicles for CO_2 emissions are shown in Figure 3. The average embedded CO_2 emissions from vehicle production were estimated with the simple calculation method initially proposed by Berners-Lee [14]. But his figure of 720 kg CO_2 per £1000 car price was replaced by what Ricardo published 350 kg CO_2 per £1000 car price [15].

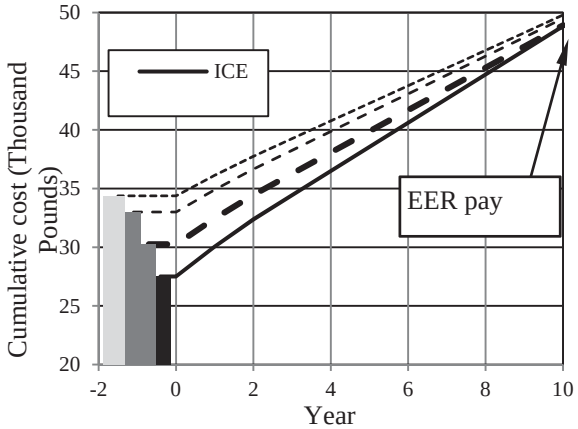

Figure 2: *Cost pay-back times for different powertrain configurations*

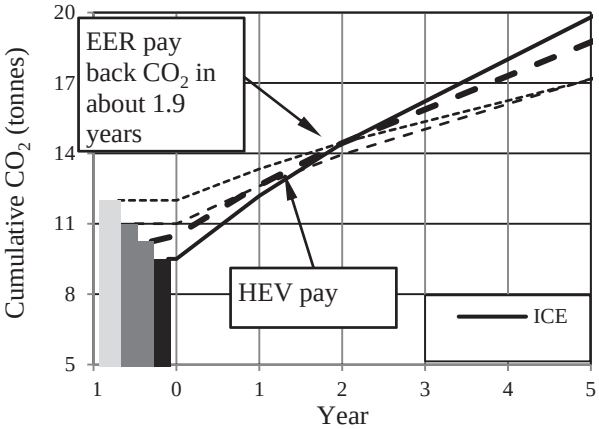

Figure 3: *CO_2 emission pay-back times for different powertrain configurations*

In Figure 3, it can be seen, with HEV vehicle's big saving rate, it could pay-back CO_2 emissions in just 1.4 years. EER need approximately 1.9 years to pay back CO_2 emissions. Because of a higher embedded CO_2 amount, HEV+EER has a similar CO_2 pay-back time as EER, though it has a fast pay-back rate. By 5 years (46000 miles), an EER vehicle could save approximately 1.1 tonnes CO_2 in average, compared to HEV's average saving of 2.6 tonnes per vehicle and HEV+EER's average saving of 2.7 tonnes. By 10 years (86000 miles), the average CO2 saving per EER vehicle could be approximately 2.8 tonnes CO_2, compared to HEV's average saving of 6.2 tonnes and HEV+EER's average saving of 7.0 tonnes.

In Figure 4, it shows the pay-back times when the increase of fuel price is taken into account. Considering the average fuel price increase of 8% in the UK in last ten years, both EER vehicles and HEV vehicles' pay-back times for cost are reduced to 8.1 years and 8.9 years. HEV+EER has a similar cost pay-back time as HEV, because HEV+EER has higher embedded cost but a higher cost pay-back rate.

In Figure 5, the analysis shows the cost pay-back times for EER vehicles could be significantly reduced to 2.7 years, if doubled mileages (24000 miles for the first year, 20000 miles for the second year and 16000 miles per year for following years) is used, compared to the average mileage used for the previous analysis. It should be noted average fuel consumptions used in this part are still same as used in the previous analysis for those four vehicle configurations, such as 0.09 litre/mile for ICE vehicles. As those high mileage operations involve more motorway driving, HEV's fuel saving rate is faded due to reduced brake regeneration etc. But EER's saving rate can be enhanced. Results shows HEV still needs at least 8.5 years for cost pay-back. But EER vehicles only need 2.7 years for cost pay-back. For this category of customers, EER vehicles would obviously be a more popular option.

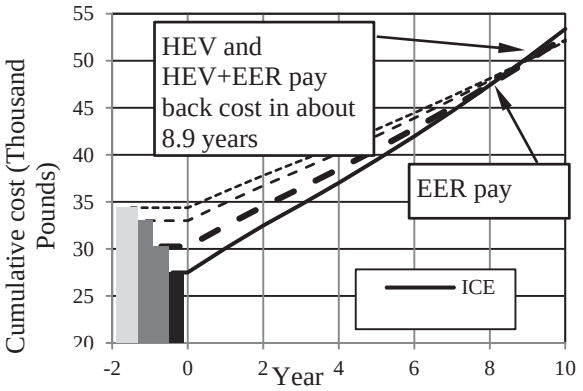

Figure 4: *Cost pay-back times of different powertrain configurations with fuel price increase 8% annually*

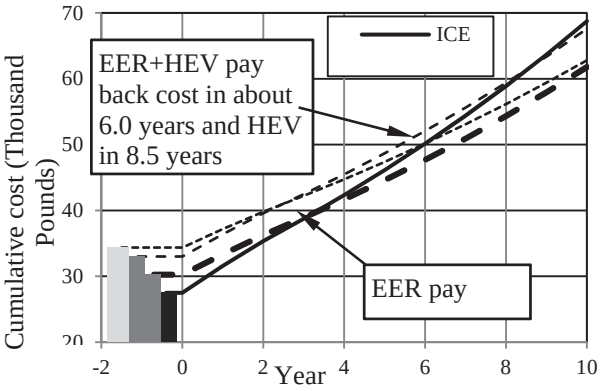

Figure 5: *Cost pay-back times of different powertrain configurations with fuel price increase 8% annually and doubled mileages*

3 Conclusion

Considering average light duty vehicle annual mileage, fuel price, other subsistence costs (such as insurance, service, tax etc.) in the UK market, an EER vehicle needs 10.1 years for cost pay-back and 1.9 years for carbon emission pay-back, compared to HEV's 11.9 year for cost pay-back and 1.4 year for carbon emission pay-back.

- When 8% annual fuel price increase is considered, the cost payback for EER vehicles is 8.1 years, compared to HEV's 8.9 years.
- Increased mileage due to more motorway driving would obviously reduce cost and carbon emission pay-back time for EER vehicles due to high EER efficiency for motorway driving. But for HEV vehicles, similar result would be difficult to achieve due to faded advantage of HEV vehicles on motorway.

References

[1] Wang T., Zhang Y. and Peng Z., A review of researches on thermal exhaust heat recovery with Rankine cycle, *Renewable and Sustainable Energy Reviews*, Vol.15(1):2862-2871, 2011.

[2] Wang T, Zhang J, Zhang Y, Shu G and Peng Z, Energy Analysis for Recoverable Exhaust Heat in a Gasoline Engine, Sustainable Thermal Energy Management in the Process Industries - SusTEM2011, Newcastle, 25th-26th October 2011.

[3] Chiong, M., Rajoo, S., and Romagnoli, A., Nozzle Steam Piston Expander for Engine Exhaust Energy Recovery, SAE Paper 2015-01-0126, 2015.

[4] Tzeng S. C., Huang K. D., Chen C. C., Optimization of the dual energy-integration mechanism in a parallel-type hybrid vehicle, *Applied Energy*, Vol.80:225-245, 2005.

[5] Teng H., Regner G. and Cowland C., Waste Heat Recovery of Heavy-Duty Diesel Engines by Organic Rankine Cycle Part II: Working Fluids for EHR-ORC, SAE Paper 2007-01-0543, 2007.

[6] Chammas R. E. and Clodic D., Combined Cycle for Hybrid Vehicles, SAE Paper 2005-01-1171, 2005.

[7] Hendricks T. J. and Lustbader J. A., Advanced Thermoelectric Power System Investigations for Light-Duty and Heavy Duty Applications: Part I, Proceedings of the 21st International Conference on Thermoelectrics, IEEE, Long Beach, CA, 2002.

[8] Yang, C., Xie, H., and Zhou, S., Efficiency Analysis of the Rankine Cycle System Used for Engine Exhaust Energy Recovery under Driving Cycle, SAE Paper 2014-01-0671, 2014.

[9] Martins, J., Goncalves, L., Antunes, J., and Brito, F., Thermoelectric Exhaust Energy Recovery with Temperature Control through Heat Pipes, SAE Paper 2011-01-0315, 2011.

[10] Wijewardane, A. and Stobart, R., Addressing the Heat Exchange Question for Thermo-Electric Generators, SAE Paper 2013-01-0550, 2013.

[11] Car Insurance Information, Average Annual Car Miles UK, available online http://www.car-insurance-information.org/average-annual-car-miles-uk.html.

[12] NREL, NREL Estimates U.S. Hybrid Electric Vehicle Fuel Savings, available online www.nrel.gov/news/press/2007/518.html.

[13] Ting C.-C., Tsai D.-Y., Hsiao C.-C., Developing a mechanical roadway system for waste energy capture of vehicles and electric generation, *Applied Energy*, Vol.92:1-8, 2012.

[14] Berners-Lee M, How bad are bananas?: the carbon footprint of everything, ISBN: 1846688914, London, 2010.

[15] Ricardo plc, Ricardo study demonstrates importance of whole life vehicle CO2 emissions, available online www.ricardo.com/ru-RU/News--Media/Press-releases/News-releases1/2011/Ricardo-study-for-Low-Carbon-Vehicle-Partnership-demonstrates-importance-of-whole-life-vehicle-CO2-emissions/.

Thermal Modelling Results for Earth Energy Bank Storage Using PV Thermal Panels Applied to Buildings

Andrew Wright[a]

[a] Institute of Energy & Sustainable Development, De Montfort University, Leicester, LE1 9BH, UK
* Corresponding author. Email: awright@dmu.ac.uk; Tel. +44(0) 116 257 7960

Abstract
This paper considers the potential for inter-seasonal earth storage of solar heat for low carbon heating, through modelling. Solar energy is plentiful in summer but scarce when heating is needed, so long-term storage of heat is required. One approach is to store heat in the ground underneath a building in a relatively small volume with several shallow, inexpensive boreholes. Heat can be provided from hybrid PV-thermal panels, which operate at low temperatures suitable for earth storage. A simple hourly model is described and some results exploring sizing and thermal parameters presented, for a well-insulated house and a small factory building. The modelling shows that system performance is strongly affected by building size and shape, with the system better suited to a factory, and the insulation of the earth store is important. Greater store depths reduce peak temperature but also increase heat loss to ground, and store heat loss to ground can easily exceed usefule heat output. Sufficient storage can be provided with depths around 2 m.

Keywords earth; ground; storage; building; solar; heat.

1 Introduction

In order to mitigate the effects of climate change, there is growing pressure to decarbonise the energy system and use more renewable energy, thus reducing the burning of fossil fuels and consequent carbon dioxide emissions. Solar energy is already widely used to generate electricity, mainly with photovoltaic (PV). In higher, temperate altitudes such as Europe and Scandinavia, there is much more solar energy available in summer than winter. However in most buildings, space-heating demands are mainly during colder months (typically Sept/October to April/May). Most buildings have a fairly steady year-round hot water demand. Heat demands in industry vary enormously, but for processes are typically fairly constant over the year, while space heating will only be required in colder months.

1.1 Types of storage

Heat and/or 'coolth' (for cooling) can be stored over varying time periods, and most of the physics applies to both. However as the focus of this paper is use of solar heat, only heat storage is considered here. Thermal storage provides a solution to the temporal mismatch between the supply and use of solar heat [1]. Many types of thermal storage are available including sensible, latent and chemical [2] but sensible heat is the most common and cheapest. To store interseasonal heat for buildings or industry, there are several types of sensible storage: boreholes, aquifers, water/gravel pits, rock stores, underground ducts, and water tanks are the most widely reported [3].

Another option is a concentrated, relatively shallow earth store beneath the footprint of a building – this is known as an earth energy bank (EEB). The amount of heat that can be stored is the product of the heat capacity of the medium, density, the volume of the store and the maximum temperature rise. A store can be constructed by drilling holes into the ground, and dropping in a matrix of vertical pipes linked at the surface by horizontal piping. Insulation of the upper surface is provided by the insulated floor of the building, and at the sides by dropping vertical insulation into a trench around the edge. The lower horizontal boundary is normally uninsulated, though insulation is possible if the whole volume is excavated first. This system has much less thermal contact with the surrounding ground than a ground source heat pump borehole system, but considerably more than an insulated tank.

1.2 Solar heat collection

Photovoltaic-thermal, abbreviated to PVT, panels can be used to produce relatively low temperature heat (up to about 50°C, but they are much more efficient at lower temperatures) and electricity.

Photovoltaic efficiency falls linearly as the temperature increases, by (according to calculation) about 0.5% for each degree Kelvin temperature rise (that is, if efficiency is η at temperature T (Kelvin), it will be 0.995η at temperature T+1). PVT panels can improve electrical PV efficiency because the thermal collector fluid usually keeps the cells cool. However, at times hybrid panels may stay warmer than pure PV panels would be in the same conditions, thus reducing efficiency compared to pure PV. For a detailed review see for example [4], [5].

1.3 Aims

The aim of the paper is to describe a simple modelling approach for a storage system for a dwelling and a small factory, using hourly weather data and some results from this, and use it to explore some of the key parameters such as building and store insulation, store depth and store temperatures.

2 System model for dwellings

The basis of a generic model is shown in Figure for a house size typical of the UK (the same principle applies to other buildings, but with different dimensions). In general, a unit area of the floor plan can be considered, because there will be unit area of store to whatever depth, to each unit area of roof. The system is modelled as an hourly heat balance between solar heat in, heat loss from the store, and useful heat into the building for space heating purposes when required. Heat loss from a building is a function of external areas, insulation and ventilation load, set point temperature, and external weather. Actual heat input required will be the space-heating requirement, minus solar gains and heat gains from occupants and equipment. Occupant and equipment gains can be modelled by assuming that, without space heating, they would warm the building above ambient a certain amount, usually assumed to be about 3 K.

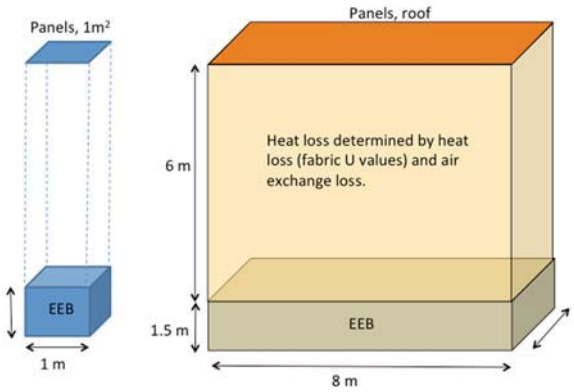

Figure 1: *Concept for generic model of solar store beneath building, for unit area (left) and building (right)*

It is assumed that the heat is perfectly distributed around the store that therefore has uniform temperature – clearly this is a simplification and there will be significant thermal lags in reality. Key parameters of the store are the heat capacity and conductivity of the material, which vary considerably. Volumetric heat capacity is the most relevant, as it can be simply multiplied by volume and maximum temperature uplift to obtain total store capacity. It is worth noting that water has 2 to 3 times the volumetric heat capacity of most soil and rock, due to its unusually high heat capacity per unit mass (which more than compensates for lower density). For example common earth has a volumetric heat capacity of 1.28 $kJ.m^{-3}.K^{-1}$, clay 1.65 $kJ.m^{-3}.K^{-1}$, granite 2.42 $kJ.m^{-3}.K^{-1}$ and water (for comparison) 4.19 $kJ.m^{-3}.K^{-1}$. Moisture content also increases thermal capacity and conductivity.

2.1 Thermal efficiencies of panels

There is no simple number for the thermal efficiency of a thermal or PVT panel, because it varies with ambient and fluid temperatures, which both dictate the rate of heat loss to surroundings. Panel manufacturers usually give peak thermal output (W), for a given fluid temperature. For example the Solar Angel DG-01 panel [6] gives a peak thermal output of 648 W. Panel test data [7] shows this is when the temperature difference between the fluid and ambient is 0 K; output is 452 W for 10 K and

55 W for 30 K difference. These are for a test standard solar flux of 1000 Wm^{-2} – more than experienced in the UK. Actual output over a year will be a function of climate and fluid temperature; collecting at a lower temperature (say 25°C rather than 50°C) will greatly increase thermal yield, but with lower exergy. Test data is provided for the Solar Angel panel for four European locations, and three collector temperatures using ScenoCalc software, reproduced here as Table – all values for 75°C were zero [7]. Data for Birmingham was also produced using the International Weather for Energy Calculation (IWEC) file, input to the ScenoCalc v4.06 software. The sunnier climates have the highest yield; Birmingham, with a rather cloudy, cool climate has the lowest yield. Low temperature collection, well suited to underground stores, appear the only useful application in European climates – also improving PV efficiency.

Table 1: *Thermal yield for Solar Angel panel (kWh per panel), five European locations*

Athens		*Davos*		*Stockholm*		*Würzburg*		*Birmingham*	
25°C	*50°C*	*25°C*	*50°C*	*25°C*	*50°C*	*25°C*	*50°C*	*25°C*	*50°C*
872	*75*	*270*	*5*	*277*	*7*	*318*	*11*	*189*	*13*

2.2 Model description

A simple model was developed for a generic building, using MS Excel. The purpose was to establish the likely temperature rise, ability to meet space-heating loads, and cyclic behaviour of heat flows in and out. The same 'average' IWEC weather data for Birmingham was used as for the panel evaluation. The input parameters were the dimensions, store material density and heat capacity, heat transmission to surrounding soil per unit area of store (assuming no heat loss from upper surface), and overall panel efficiency. Solar flux was simply calculated as horizontal radiation given in the weather file, multiplied by 1.11 to account for the slope, assumed to be optimal. The number of panels was the area of the roof multiplied by an 'availability' factor between 0 and 1, divided by total panel area, rounded down to the nearest integer. The starting value of the store is set to 14°C. Heat loss (W) from the house was calculated using the following formula:

$$Heat\ loss = f(T_o - T_B)(A.U + c_{pair}.\ n.V/3600) \text{ where } f(x)=x \text{ for } x>0,\ 0 \text{ for } x<=0. \quad (1)$$

where T_B is balance point, the outside temperature at which no heating is required; T_o is air temperature, A (m^2) is total surface area of house walls and roof, U is thermal transmittance (inverse of resistance) ($W.m^{-2}.K^{-1}$), c_{pair} is heat capacity of air 1200 $kJ.m^{-3}.K^{-1}$, n is air change rate (h^{-1}) and 3600(s) is to convert the air change rate to s^{-1}. A U value of walls and roof of 0.12 $W.m^{-2}.K^{-1}$ was used, corresponding to a very well insulated building, and air change rate *n* of 0.25 ach which corresponds to a level for adequate fresh air, for a small number of occupants, or a higher rate but with heat recovery on a mechanical system for more occupants – in either case a low heat loss for ventilation. Similarly, heat loss from the store to the surrounding soil was calculated as

$$(T_s - T_{surr})(A.U) \quad (2)$$

where T_{surr} was the ambient soil temperature taken as 11°C, *A* was the area of the sides (building perimeter multiplied by store depth) and underside (assuming negligible heat flow through the well insulated floor) and *U* was thermal transmittance; initially a value of 0.5 $W.m^{-2}.K^{-1}$ was used, corresponding to about 66 mm of polystyrene board. Heat gain (W) for each panel was calculated as

$$1.11(A_p.\ \eta.g) \quad (3)$$

where 1.11 is the slope factor, A_p is panel solar aperture, *g* is horizontal solar flux ($W.m^{-2}$) and η is panel efficiency. Based on the ScenoCalc modelling results for Birmingham, an overall thermal efficiency value of 0.17 was used. There was no limit set on the store temperature, in order to explore the behaviour fully, although in fact as temperatures rise about 30°C the efficiency of the collector will drop rapidly (Table). In reality, only scenarios with store temperatures below about 30°C would work effectively for this type of collector.

2.3 Results simple model - house

An hourly model was used, but for ease of plotting converted to daily values using pivot tables. One scenario is shown in Figure , for scenario F in Table. The store temperature falls to below 3°C in early

March, and rises to nearly 30°C in late September (about a month later than the peak air temperatures), but falls again to finish close to its starting value of 14°C.

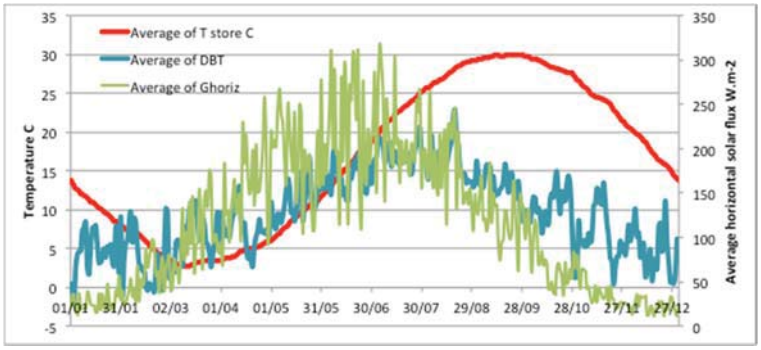

Figure 2: *Daily averages of air temperature, thermal store temperature and solar flux over 1 year, scenario F in Table; DBT is external Dry Bulb Temperature, Ghoriz is global horizontal solar radiation*

Parameters were varied with the aims of achieving a modest depth (< 3m), final temperature close to initial, and maximum store temperature below 40°C. Some example scenarios are shown in Table. It was found impossible to stop the store temperature falling over the year when the store U value was 0.5 $W.m^{-2}.K^{-1}$ or above; the smallest fall was found for around 6.5 m store depth (A). Reducing the store U value to 0.4 makes no net change in store heat over the year possible (i.e. same start and end temperatures), with a reduced 4m depth (B), but heat loss from the store is still more than three times the heat loss from the house (the 'useful' application of the heat). Further store U value reduction to 0.3 makes a store depth of only 1.15m possible, but with a very high peak temperature, unrealistic for this type of panel (C). Increasing the depth to 3m reduces the peak but with a large rise in store temperature (D). Improving store U value further allows a depth of 1.7m and a low peak temperature, with no annual temperature change, and store heat loss only 17% higher than house loss. Finally (F) shows a roof fraction of only 0.3 is possible, with low peak temperature and small store heat loss just 27% of the house heat. These results show that it is critical to size all parts of the system to achieve satisfactory results.

Table 2: *Effect of store depth, store U value and roof fraction on daily average store temperatures and store heat loss over year; house thermal properties remain constant*

Scenario	*A*	*B*	*C*	*D*	*E*	*F*
Store U value	*0.5*	*0.4*	*0.3*	*0.3*	*0.2*	*0.1*
Roof fraction	*1.0*	*1.0*	*1.0*	*1.0*	*1.0*	*0.32*
Depth store m	*6.0*	*4.0*	*1.15*	*3*	*1.7*	*2.0*
Max store temperature	*24.6*	*33.7*	*76.2*	*45.9*	*43.3*	*30.1*
Final store temperature	*12.1*	*13.8*	*13.8*	*7.9*	*14.0*	*13.73*
Change in store temp.	*-1.8*	*-0.1*	*-0.15*	*3.90*	*-0.02*	*-0.25*
Store loss kWh	*5771*	*5568*	*5552*	*5325*	*1945*	*452*
House loss kWh	*1661*	*1661*	*1661*	*1661*	*1661*	*1661*
Ratio store/house	*3.47*	*3.35*	*3.34*	*3.21*	*1.17*	*0.27*

The ratio of total heat flow into store (summing positive flows in) divided by maximum heat stored (i.e. store temperature at peak) was found to be around 2.5 to 2.9, where there is negligible loss of heat over a year. This is significant – it means that the simply considering the maximum storage capacity is misleading, because there is a lot of cyclic heat input and output (useful and losses) as well as the overall annual cycle. This ratio provides a sort of useful 'gearing' of capacity of about 2.5.

2.4 Results for factory building

A model run was also done for a factory building with the inputs shown in Table , including less insulation and higher air change rate which is more realistic for this type of building. With these inputs, the final temperature almost equals the start temperature; peak daily store temperature is 36.2°C, achievable with a low temperature collector. This shows that due to the different geometry, with less heat loss relative to store volume and greater storage capacity per unit roof area, target performance can easily be achieved for lower thermal standards and panels on only 39% of the roof.

Table 3*: Inputs for factory building*

Length (m)	*Width (m)*	*Height (m)*	*U building* $W.m^{-2}.K^{-1}$	*U store* $W.m^{-2}.K^{-1}$	*Air change* h^{-1}	*Depth store (m)*	*Roof fraction*
50	20	6	0.25	0.2	0.25	2	0.39

3 Conclusions

For inter-seasonal storage, an earth energy bank beneath a building provides an interesting alternative to the more common water tank and borehole systems. PVT panels appear to provide an appropriate low temperatures input. A simple model has been developed to explore the parameters of building geometry, building and store insulation, and store depth for a central UK climate. This ignores dynamic effects within the store but still provides some useful insights. Insulation of the store is found to be very important. Building size also has a large impact on overall performance, primarily because of the higher ratio of store volume and solar collection area to heat loss. It is quite easy to achieve adequate storage for a small factory, even with relaxed thermal standards, but harder (in terms of insulation and proportion of roof with collectors) for a house. A factory may also have waste process heat that can be added to the store, in which case a larger store may be appropriate. More detailed modelling would be needed to establish behaviour more accurately, particularly in relation to thermal dynamics within the store, heat flows at the lower boundary, and to quantify the improvements in PV efficiency. Nevertheless, these results do indicate the importance of correctly sizing the store and collectors in relation to the thermal properties of the building and store itself. It is also shown that total flow into the store (which equals flow out if balanced) is two to three times greater than the maximum store capacity.

References

[1] Heier J, Bales C and Martin V 2015 Combining thermal energy storage with buildings – a review *Renew. Sustain. Energy Rev.* 42 1305–25
[2] Xu J, Wang R Z and Li Y 2013 A review of available technologies for seasonal thermal energy storage *Sol. Energy* 103 610–38
[3] Hesaraki A, Holmberg S and Haghighat F 2015 Seasonal thermal energy storage with heat pumps and low temperatures in building projects—A comparative review *Renew. Sustain. Energy Rev.* 43 1199–213
[4] Abdul Hamid S, Yusof Othman M, Sopian K and Zaidi S H 2014 An overview of photovoltaic thermal combination (PV/T combi) technology *Renew. Sustain. Energy Rev.* 38 212–22
[5] Chow T T 2010 A review on photovoltaic/thermal hybrid solar technology *Appl. Energy* 87 365–79
[6] SolarAngel DG-01 Solar Angel DG-01 Specification sheet 1–2
[7] SP 2014 Solar Keymark Certificate.

Influence of the Optimal Storage Tank Capacity on the Economy of Hybrid PV Micro-CHP Systems

Massimiliano Renzi[a*], Caterina Brandoni[b]

[a] Faculty of Science and Technology, Free University of Bolzano, Bolzano, 39100, Italy
[b] Centre for Sustainable Technologies, School of the Built Environment, University of Ulster, Newtownabbey, Co Antrim BT370QB, UK
* Corresponding author. Email: massimiliano.renzi@unibz.it; Tel. +39 (0)471 017816; Fax. +39 (0)471 017009

Abstract
Hybrid renewable systems, made up of a PV unit and a micro-Combined Heat and Power technology can help to cope with the intermittency of solar energy, reducing the stress on the distribution electricity grid, while reducing the emissions of the building sector. However, the introduction of such technologies seeks an optimal approach in order to maximise their competitiveness with respect to fossil fuel generation. The present paper focuses on the use of water storage tanks to enhance the economy of hybrid renewable systems through the analysis of the influence of the main design parameters on its optimal size, such as: i) natural gas prices, ii) electricity prices, iii) capital costs. For micro-generation applications in the residential sector, results show as the positive contribution of TES is evident in case of a higher operational flexibility, such as with a Time of Use electricity Tariff. The outcome suggests as a higher flexibility in the energy tariff system can help the economy of micro-generation systems.

Keywords micro-generation; optimal sizing; micro-CHP; PV; thermal storage; energy savings.

1 Introduction

In most of the developed Countries the building sector plays a significant role in the final energy consumption [1]. Most of the share of the building sector energy consumption is ascribable to dwellings that in the EU-27 account for about 26% of the total consumption [2]. Therefore, there is a significant scope to reduce the energy impact of buildings by introducing proper measures and targets such as minimum energy performance standards, construction of net-zero energy consumption buildings, improvement of energy efficiency in existing buildings and introduction of renewable energy systems. With particular focus on this last point, PhotoVoltaic (PV) market has shown a steep growth and, thanks to the economies of scale and the feed in tariffs, the investment cost for this technology has dropped down to about 2,200 €/kWp in 2014 also for small scale residential applications [4]. PVs are particularly suitable for building integration, thanks to the large availability of the solar source and their easy installation on new and existing buildings. One of the critical issues that have emerged in the integration of solar PV systems into the electricity grid is determined by the unpredictable nature and intermittency of the solar resource [5]. The authors of the present study have already investigated in a previous paper [6] a promising opportunity to overcome these problems which is the introduction of hybrid systems. Hybrid systems consist of coupling alternative energy systems with other distributed generation units fed by traditional fossil fuels. Distributed generation systems are typically operated in cogeneration mode, which means a combined production of heat and power (CHP). The application of hybrid systems should allow a deeper PV deployment if compared to a conventional centralized electric generation system [7]. The use of a Combined Heat and Power (CHP) system in the building sector involves significant problems that are still to be solved due to the mismatch of the thermal and electric loads. A possible solution for a better management strategy lies in the introduction of Thermal Energy Storage (TES) systems. TES systems provide the opportunity to store thermal energy by heating a storage medium: therefore, energy can be used at a later time. TES systems are particularly suitable for buildings and industrial processes where a significant share of the user demand is in the form of thermal energy, with sudden and steep variations during the days and from one day to another. Therefore, if properly managed, TES are also able to reduce energy consumption, emissions and system costs. At present, it is possible to mention three typologies of TES systems: i) sensible heat storage, based on heating a liquid or solid storage medium, being water the easiest and most common solution; ii) latent heat storage by adopting phase change materials; iii) thermo-chemical storage by using chemical reactions to store thermal energy. Among the aforementioned solutions, sensible heat storage is the

cheapest and most mature technology; it can be easily embedded in domestic systems, but also in district heating and industrial plants. On the contrary, this technology requires larger storage volumes due to its lower energy density and a proper system design is required to supply thermal energy at constant temperatures. Hot water systems for domestic applications are usually in the range of 0.5 to several m^3 and can be used for daily storage. Typical charging temperatures are in the range of 80-90°C while their efficiency can be up to 90% if good insulation is applied to the storage tank and high specific heat medium is used. A complete system for TES has a cost ranging from €0.1-10/kWh, being the upper limit referred to small systems with high efficiency thermal insulation technology [8]. A hybrid system that embeds renewable energy devices, CHP units and TES might have a significant investment cost; therefore, a proper optimization of the system size is required in order to be competitive with conventional fossil fuel energy generation. The evaluation of the optimal sizing of the single components of the hybrid system is a complex issue since several parameters must be taken into account, such as electricity, fuel price, and energy loads [9].

There are several techniques that can be adopted for the optimal sizing algorithm; the present paper uses a linear programming technique, taking advantage of the rapid calculations. This technique has been already used in literature for sizing small-scale CHP systems [10]. The focus of the work is on the optimal size of the water storage tank and of the additional hybrid system components, such as the micro-CHP and PV unit, in order to enhance the economy of hybrid renewable systems. A sensitivity analysis, aimed to investigate the influence on the main design parameters, is also presented. In details, session 2 and 3 describe, respectively, the systems modelling and the optimal algorithm developed; session 4 discusses the simulation results and findings of the work.

2 Material and methods

The system proposed in this study is intended to meet the energy requirements of a residential application. The conceptual lay-out of the system under analysis is composed of a solar PV system, a micro-CHP device (the technologies considered in this study are Internal Combustion Engines, ICE, Stirling Engines, SE, and Fuel Cells, FC), a TES device and a cooling device (vapour compression chiller or water/LiBr absorption chiller). The lay-out of the hybrid system has been considered for providing the maximum possible flexibility. Electric loads can be met by the PV system or by the micro-CHP unit or electricity can be bought from the grid. Instead, either the CHP unit, or the auxiliary boiler or the TES satisfies the thermal demand. Finally, the cooling demand is met by the absorption chiller or the vapour compression chiller.

2.1 Solar system modelling

The performance of the PV system is strongly dependant on the conditions of the place where it is installed. Therefore, the data of a Typical Meteorological Year (TMY) of the considered location have been used. In particular, in order to model the solar device, the hourly trend of the global solar irradiation over a south-oriented 30° tilted surface (global tilted irradiation, which is the optimized tilt for the Italian latitudes) and the ambient temperature have been used. In fact, the efficiency of a PV panel is strongly dependent on the available solar radiation and the solar cell temperature. The model that is better described in [6], calculates the PV panel efficiency as a function of the panel temperature and the available irradiation. Also the balance of system losses (BOS) are taken into account. Table 1 reports the nominal parameters of the PV system used in this work.

Table 1: *Main performance parameters of the PV module*

Parameter	*Value*
Cell Type	*Polycristalline silicon solar cell*
Module model	*Sharp ND-R240A6*
Module power (STC)	*240W*
Module electrical efficiency (STC)	*14.6 %*

2.2 Micro-CHP modelling

As mentioned in the introduction, three technologies were taken into account in this study: ICEs, Stirling engines and fuel cells. All these devices have been modelled considering their main nominal performance parameters, namely electric efficiency and thermal efficiency.

Table 2 shows the main parameters used in the analysis that describe the behaviour of commercial units already available in the market. The electric efficiency of the devices is considered constant with the aim to take advantage of linear programming techniques. A better description of the characteristics of the single devices is reported in [6].

Table 2: *Main nominal parameters used for modelling micro-CHP devices and chillers*

Micro-CHP unit			
	ICE	Stirling	Fuel cell
Electrical efficiency [%]	24	15.8	40
Thermal efficiency [%]	64	75	40
Power to heat ratio	0.38	0.2	1
Specific cost [€/kWe]	3400	4500	6700
O&M COST	0.021	0.017	0.019
Lifetime		- -10 year- -	
Chiller unit			
	Compression chiller	Absorption chiller	
COP	3	0.7	
Lifetime	- - 10 year - -		
Specific cost [€/kW]	250	300	

3 Optimal sizing of the hybrid system for the test case

The main aim of the proposed algorithm is to satisfy the requirements of the user following a minimum total annual cost criterion. In order to do so, a typical day for each season has been modelled with a time step of one hour; results have been then extended for the entire year. Other simplifying considerations are that the output of the CHP devices can range from zero to the nominal power and that the O&M costs of the TES are negligible. The procedure also takes into account a series of constraints that are mainly related to the hourly energy balances of the single devices involved in the hybrid system. The described algorithm has been used to study a test case of a dwelling in Rome, central Italy, whose energy loads are shown in Figure 1.

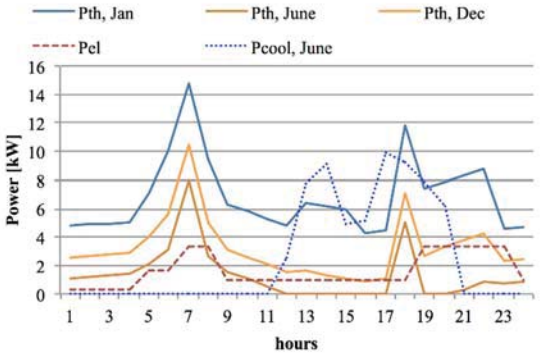

Figure 1: *Energy load of the case under study*

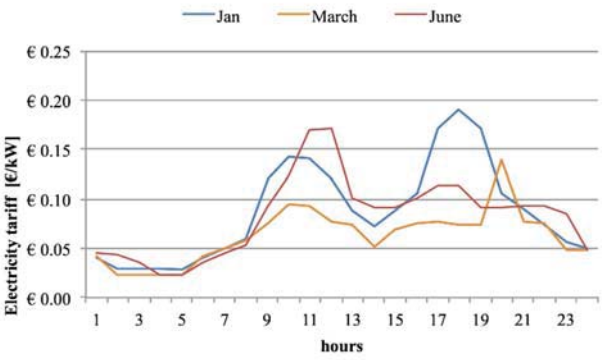

Figure 2: *TOU tariff considered in the analysis*

Both a flat electricity tariff of 0.16 €/kWh and a variable tariff, following a daily market trend, have been chosen (Figure 2). For the latter, costs of distribution and dispatch have been added in order to reach the same average value of the flat tariff and correctly compare the two cases. As discussed in [11], indeed, the use of a Time Of Use (TOU) tariff can increase the attraction of water storage tanks.

Moreover a sensibility analysis of both electricity and Natural Gas, NG, tariff (15% higher and lower of the reference value) has been developed.

4 Results and discussion

Figure 3a shows the size of the micro-CHP unit and TES defined by the optimal sizing procedure, together with the yearly savings of the hybrid renewable energy system compared to the traditional energy generation. The savings, without the introduction of a TES, are also reported in order to understand the contribution coming from the TES unit. It is worth noting that the PV system is always sized at its upper limit, which, in the present analysis, has been set equal to the electric peak demand. Since the current cost of the fuel cell is too high, the algorithm selects this micro-CHP technology only if the capital cost is reduced down to 3500€/kW_e (case reported as FC*).

For the case study under analysis, the algorithm chooses the TES only for the ICE and the FC* case. The technologies are sized at an electrical output of 0.3kW_e and 0.5kW_e, respectively. In both cases the number of operating hours of the micro-CHP technologies increases and the TES helps in meeting the thermal energy demand with a lower total cost. For the SE case, the optimal procedure does not select the TES. The optimal size of the Stirling Engine unit is 0.3kW and the immediate use of the recovered thermal energy provides the most economic management strategy.

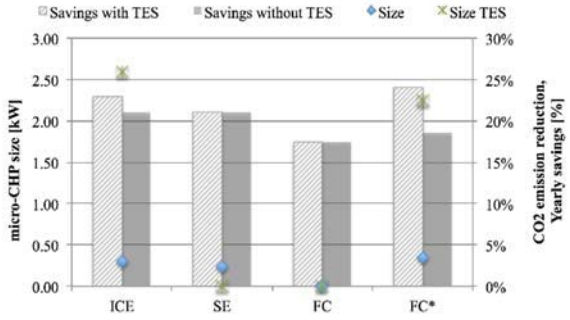

Figure 3(a): *Size of micro-CHP unit and TES;*

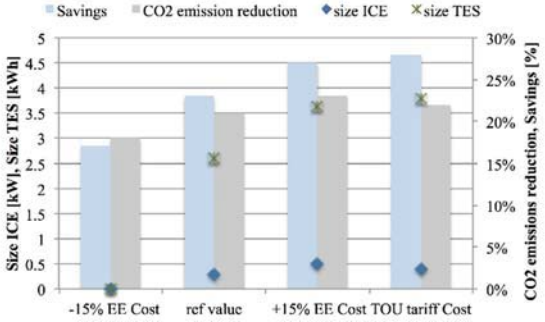

Figure 3(b): *Size of the ICE and the TES, savings and CO2ER for the hybrid system with an ICE*

Figure 3b shows the case of the ICE that is recognised to be the most advantageous micro-CHP technology in residential applications [5]. A higher electricity tariff increases the attraction of TES, as expected. In this case, the cost of the electricity produced by the cogeneration system becomes, indeed, cheaper than the electricity bought from the grid. The use of TOU tariff also promotes the use of the TES with a direct advantage on the economy of the overall system. Figure 4 shows the savings, CO_2 emission reduction and the sizes of both the micro-CHP unit and the TES for both ICE (Figure 4a) and SE (Figure 4b) in case of different NG tariffs. A reference NG tariff of 0.046€/kWh has been used in the analysis. A reduction in the NG tariff improves the economy of the hybrid system. For the ICE case, the number of operating hours increases as well as the TES capacity to store the heat in excess produced by the CHP system. Differently, for the SE technology, there is an increase in the size of the TES, but the number of operating hours of the unit decreases. The higher savings, in this case, derive from a lower number of operating hours at which the system works at partial load.

Finally Figure 5 shows the influence of reducing the capital cost of both micro-CHP and TES compared to the reference case for both ICE and SE. A reduction in the cost of the TES can enhance the economy of hybrid systems, although the extra-savings for a dwelling application is in the range 2-4%. More important reductions can come from the reduction in the capital cost of the micro-CHP unit, in particular for the SE technology, whose cost represents one of the main barriers to its deployment.

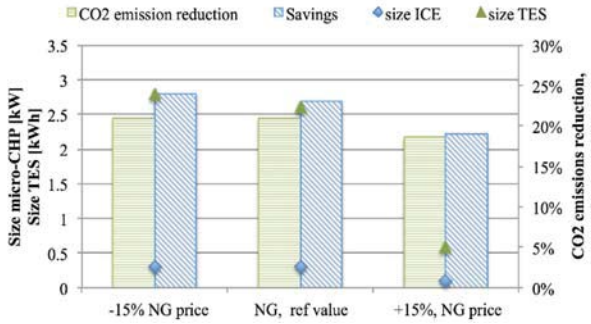

Figure 4(a): *Savings, CO2ER, size of TES and of micro-CHP unit for the ICE case*

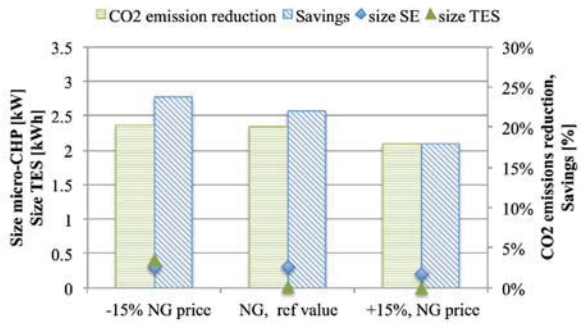

Figure 4(b): *Savings, CO2ER, size of TES and of micro-CHP unit for the SE case*

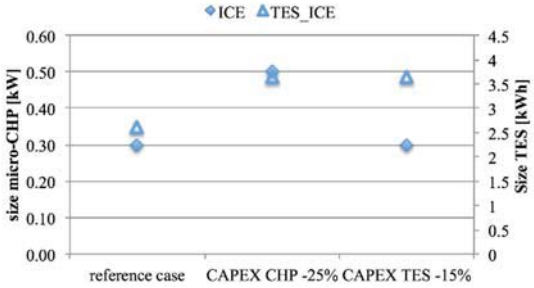

Figure 5(a): *Influence of the CAPEX on the optimal size of the system for the ICE case*

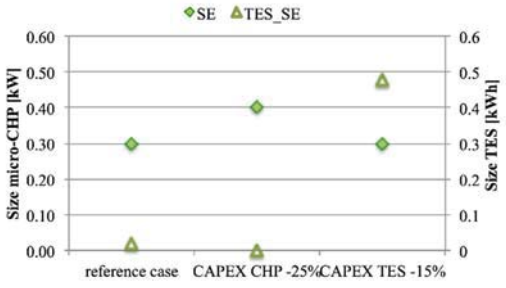

Figure 5(b): *Influence of the CAPEX on the optimal size of the system for the SE case*

5 Conclusions

The present paper has analysed the contribution of water storage tanks to the economy of hybrid renewable energy systems made up of PV and micro-CHP technology. The work represents a follow-up of a previous work written by the same authors [6]. In case of ICEs, which represent the most suitable technology for residential applications, higher savings can be achieved with a water storage unit, in particular in case of: i) a higher flexibility of the electricity tariff, ii) lower natural gas tariff that can be provided, for instance, by a reduced taxation for the fuel feeding the micro-CHP unit, as already happens in some EU countries (i.e. Italy, Germany) and ii) a reduction in the cost of storage tanks, that could be provided as grant scheme. The listed measures do not require a high investment by the Government and can help the spread of micro-generation technologies, which have been recognised as a valuable option to decarbonise the building sector.

References

[1] B.C. O'Neill, X. Ren, L. Jiang, M. Dalton, The effect of urbanization on energy use in India and China in the iPETS model, Energy Economics 34 (2012), Supplement 3(0) S339-S345.

[2] K. Vatopoulos, D.A. Johan, I.P. Carlsson, G. Zubi, Study on the state of play of energy efficiency of heat and electricity production technologies, J.S.a.p. reports, (2012).

[4] Intitute for Solar Energy Systems, ISE, Photovoltaics Report. http://www.ise.fraunhofer.de. (2014), last access: April 2015.

[5] C. Brandoni, A. Arteconi, G. Ciriachi, F. Polonara, Assessing the impact of micro-generation technologies on local sustainability. Energy Conversion and Management 87 (2014) 1281–1290.

[6] C. Brandoni, M. Renzi, Optimal sizing of hybrid solar micro-CHP systems for the household sector, Applied Thermal Engineering 75 (2015) 896–907.

[7] J.M. Pearce, Expanding photovoltaic penetration with residential distributed generation from hybrid solar photovoltaic and combined heat and power systems, Energy 34 (2009) 1947-1954.

[8] International Renewable Energy Agency, Thermal Energy Storage: Technology Brief, IEA-ETSAP and IRENA© Technology Brief E17 – January 2013, Available at www.irena.org/, last visited on May the 1st 2015

[9] J. Wu, J. Wang, S. Li, Multi-objective optimal operation strategy study of micro-CCHP system. Energy 48 (2012) 472-483.
[10] O.A. Shaneb, G. Coates, P.C. Taylor, Sizing of residential μCHP systems. Energy and Buildings 43 (2011) 1991-2001.
[11] H. Ren, W. Gao, Y. Ruan, Optimal sizing for residential CHP system, Applied Thermal Engineering 28 (2008) 514–523.

Improving Thermal Stability of Solid Acid Electrolytes for Low Temperature Fuel Cells

Berceste Beyribey[a]*, Emre Günay[a], Berrin Saygı[a,b], Burcu Çorbacıoğlu[a] and Hanifi Saraç[a]

[a] Chemical Engineering Department, Yildiz Technical University, TR-34210 Istanbul, Turkey
[b] Department of Chemical and Process Engineering, Yalova University, Yalova, Turkey
* Corresponding author. Email: berceste@yildiz.edu.tr; Tel. +90 212 383 4753; Fax. +90 212 383 47 25

Abstract

$x CsH_2PO_4 \cdot (1-x) Te(OH)_6$ composites have been synthesized for the different compositions (x=0,2-0,8). The synthesized composites were characterized by Scanning Electron Microscopy (SEM), X-Ray Diffraction (XRD), Termogravimetry (TG) and Differential Thermal Analysis (DTA). Our observations indicate that telluric acid ($Te(OH)_6$) added to cesium dihydrogen phosphate (CsH_2PO_4) significantly effects the structure, particle size and thermal stability of the composite material. Enhancing the thermal stability would be the key driver for CsH_2PO_4 to be used as electrolyte in low temperature fuel cells.

Keywords solid acids; low temperature fuel cells; thermal stability; characterization.

1 Introduction

Solid acids are compounds which show properties between that of a normal acid and a normal salt. Cesium dihydrogen phosphate, CsH_2PO_4, is one of the members of potassium dihydrogen phosphate (KH_2PO_4-type) family. Under sufficient humidification, CsH_2PO_4 transforms from a monoclinic to a stable, cubic phase at 228 °C and 1 atm total pressure and exhibits high proton conductivity ($>10^{-2}$ Scm^{-1}) above this phase transition, known as the superprotonic phase transition [1, 2]. Due to its high conductivity in the superprotonic state and relatively high decomposition/melting point (ca. 200-230 °C); CsH_2PO_4 has become an attractive candidate for fuel cells operating at low and intermediate temperatures.

However, conditions limit the temperature range superprotonic phase transition in CsH_2PO_4. Under dry conditions, it decomposes to form polymerization products at temperatures above 200 ºC [2-5] and its conductivity decreases dramatically.

$$CsH_2PO_4 \rightarrow \tfrac{1}{2}\, Cs_2H_2P_2O_7 + \tfrac{1}{2}\, H_2O \rightarrow CsPO_3 + \tfrac{1}{2}\, H_2O \quad (1)$$

The narrow temperature range and chemical instability of the superprotonic phase limits CsH_2PO_4 use in fuel cell applications. Therefore, stabilization of the high conductive phase at a wide temperature range is very important for practical uses of CsH_2PO_4.

In this study, we have investigated the effect of telluric acid addition into CsH_2PO_4 on thermal stability.

2 Experiment

Five different composition of $x CsH_2PO_4 \cdot (1-x) Te(OH)_6$ (x=0.02, 0.04, 0.05, 0.06 and 0.08) were synthesized. The synthesized composites have been mentioned as composite A, B, C, D and E, respectively. All starting reagents were commercially purchased and used without further purification. In all synthesis, required amount of telluric acid (H_6TeO_6) (99%, Fluka) and cesium carbonate (Cs_2CO_3) (%99.9, Sigma-Aldrich) were dissolved in a minimum amount of distilled water, separately. The phosphoric acid (H_3PO_4) (85 wt. % in H_2O, Sigma-Aldrich) solution was stoichiometrically added to the cesium carbonate solution. The resulting solution was stirred for one hour and then added into H_6TeO_6 solution. The mixed solution was evaporated slowly at approximately 65 ºC overnight and the obtained gel-like product was kept in an oven at 110 ºC for 2 days.

3 Results and discussions

Fig. 1 demonstrates the SEM images of the synthesized $x CsH_2PO_4 \cdot (1-x) Te(OH)_6$ composites (x=0.02, 0.04, 0.05, 0.06 and 0.08). The composite A is the one including the most amount of telluric acid as having a $CsH_2PO_4/Te(OH)_6$ molar ratio of 1:4. 1000X magnificated images of the composite A can be

seen in Fig. 1a. The amorphous and larger particles in the range of 10-20 micron might be CsH_2PO_4 considering it occurs from the atoms with larger diameters than that of $Te(OH)_6$. 1-5 micron size particles' structure is in good agreement with the monoclinic structure of $Te(OH)_6$. The composite B with a $CsH_2PO_4/Te(OH)_6$ molar ratio of 2:3 has smaller particles in size than the composite A (Fig. 1b). Decreasing the telluric acid amount in the composite might cause the smaller particle size in the composite, as well as an unrequired side product can be responsible of the change in both particle size and structure. In the composite B, instead of the amorphous and monoclinic structures obtained in the composite A, the platelet/stick shaped anortic structures take the place of amorphous and monoclinic ones. As seen in Fig. 1c, the structure in the composite C becomes amorphous with an equal molar ratio of $CsH_2PO_4/Te(OH)_6$ and the nanoparticles are also seen on the surface of the amorphous structure. As is clear from the Fig. 1d, increased $Te(OH)_6$ amount in the composite enhances the amorphous structure. The composite E, which has a $CsH_2PO_4/Te(OH)_6$ molar ratio of 4:1, is the composite with the highest $Te(OH)_6$ content and even the amorphous structure dominates in the composite, it might be said that a crystalline structure start to be formed again at this $CsH_2PO_4/Te(OH)_6$ ratio.

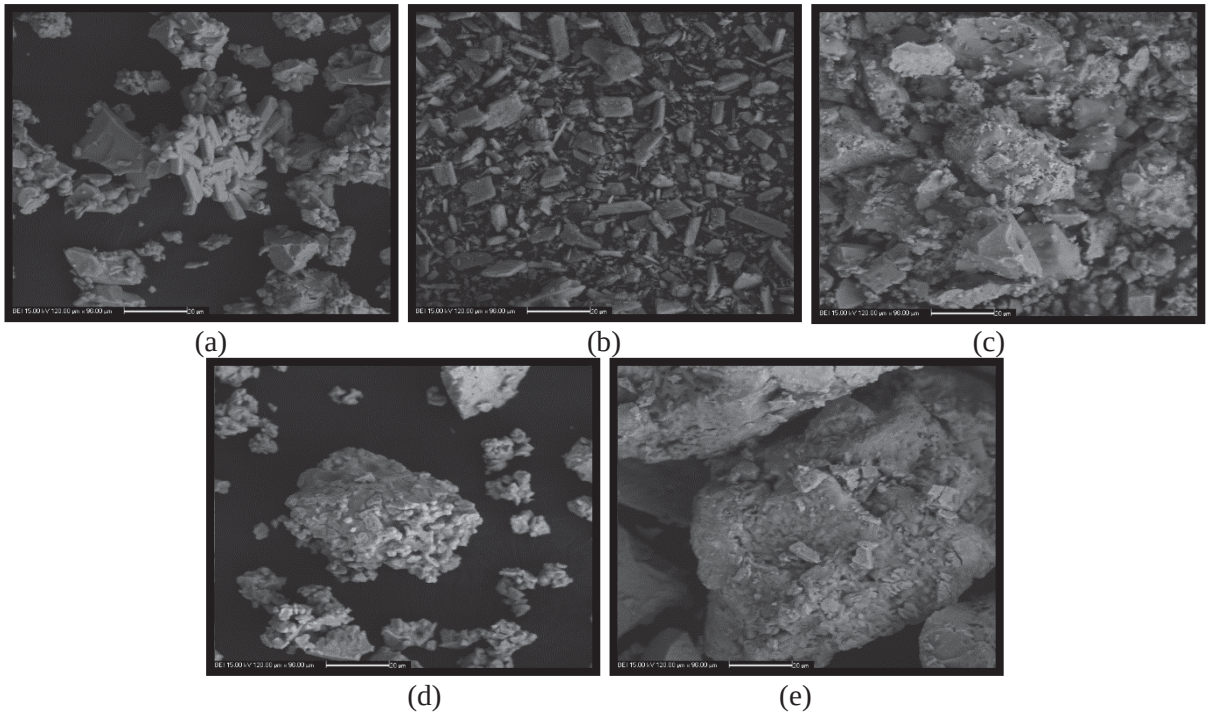

Figure 1: *SEM images of the synthesized $xCsH_2PO_4 \cdot (1-x)Te(OH)_6$ composites for 1000X and 4000X magnifications (Composite A; x=0.02, Composite B; x=0.04, Composite C; x=0.05, Composite D; x=0.06, Composite E; x=0.08)*

Figure 2 reports the XRD results of the synthesized $xCsH_2PO_4 \cdot (1-x)Te(OH)_6$ composites. The XRD result of the composite A does not indicate any crystalline structure in the composite and presents an amorphous structure (Fig. 2a). However, SEM result of the composite A clearly shows the presence of monoclinic structure besides the amorphous one. This occurrence can be explained by the broad peak of the amorphous structure between 23-33º might block the peaks from the crystalline structure. The composite B is the only composite shows no presence of an amorphous structure (Fig. 2b) and in good agreement with $Cs_3P_3O_9 \cdot H_2O$ structure. The temperature control problem with hot plate heaters might be responsible of that formation of the undesired $Cs_3P_3O_9 \cdot H_2O$, as solid acids can be easily dehydrated to their other side products. 5-10 °C decrease in the evaporation temperature can sort the formation of the side products out. $Cs_3P_3O_9 \cdot H_2O$ formation have not been seen in other $xCsH_2PO_4 \cdot (1-x)Te(OH)_6$ composites. The amorphous structure dominates the structure in the composite C (Fig. 1c), however the sharp peak around 44-45° indicates the presence of a crystalline structure, which might be attributed to the presence of CsH_2PO_4 or the formation of side products like TeO_2 or Te_2O_5. Amorphous structure without any presence of crystal structure is seen in the composites D and E.

Figure 3-7 give the thermal analysis of the synthesized composites. All analysis were carried out in nitrogen between room temperature and 500 °C with Perkin Elmer Diamond system at a scan rate of 5 °C min^{-1} in heating cycle and that of 10 °C min^{-1} in cooling cycle. Cooling of the all composites were interrupted due to an unknown reason occurred in the thermal analysis system.

As seen in Figure 3a, an endothermic slight peak is seen around 30 °C with a mass loss of 0.25%. This weight loss is related to the release of humidity. Heating above this temperature, the crystallization of CsH_2PO_4 occurs till 133 °C. An unusual weight loss of 1.6% through the crystallization process can be attributed to the release of water from the surface of the compound (like $CsH_2PO_4 \cdot xH_2O$). Neither endothermic nor exothermic peak is seen in DTA analysis over the crystallization process. This might be attributed to the existence of slow crystallization process and a clearer DTA analysis can be observed at higher scan rates than 5 °C min^{-1}. The weight loss above 133 °C is likely due to the melting of telluric acid and this observation is in good agreement with the melting point of telluric acid (136 °C). The fast weight loss which occurred at 330 °C is ascribed to the melting of CsH_2PO_4 (345 °C).

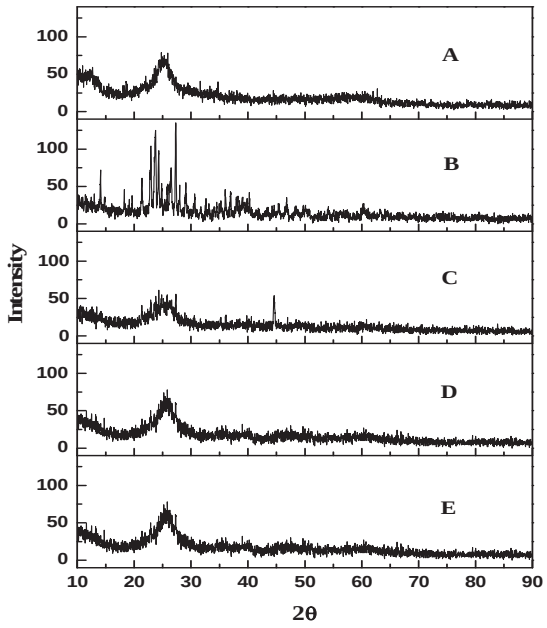

Figure 2: *XRD results of the synthesized $xCsH_2PO_4 \cdot (1-x)Te(OH)_6$ composites (Composite A; x=0.02, Composite B; x=0.04, Composite C; x=0.05, Composite D; x=0.06, Composite E; x=0.08)*

Figure 3b gives the thermal analysis of the composite B. The crystalline structure of the composite B is previously identified as $Cs_3P_3O_9 \cdot H_2O$ with XRD results. The weight loss above 139 °C with an endothermic peak around 142 °C is defined as melting of telluric acid. Above 289 °C, the weight loss and the endothermic effect is likely the decomposition of $Cs_3P_3O_9 \cdot H_2O$. In Figure 3c, TG curve of the composite C shows two decomposition steps. The weight loss above 130 °C with a slight endothermic effect around 143 is attributed to the melting of telluric acid. Second step with an onset temperature of 336 °C is an agreement with the melting of CsH_2PO_4. It seems CsH_2PO_4 might be thermally stable in the composite C up to its melting point. In Figure 3d, the weight loss up to 131 °C is attributed to releasing surface water through crystallization. Above this temperature, melting of telluric acid and decomposition of CsH_2PO_4 are likely responsible of these decomposition steps.

As similar to the other composites, a weight loss with an onset temperature of 140 °C in the composite E is referred to the melting of telluric acid (Figure 3e). An endothermic peak at 147 °C is also in agreement with this weight loss. The other decomposition steps are attributed to the decomposition of CsH_2PO_4.

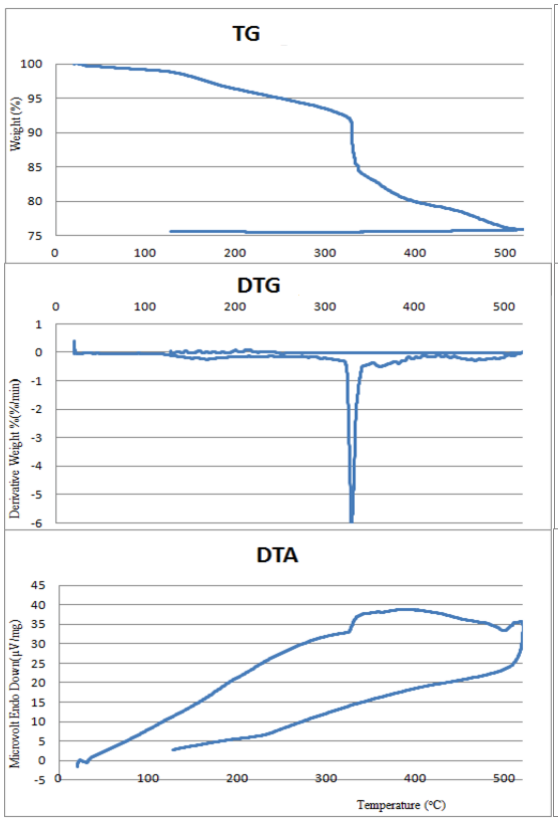
TG
Weight (%)
DTG
Derivative Weight %(%/min)
DTA
Microwolt Endo Down(µV/mg)
Temperature (°C)

(a)

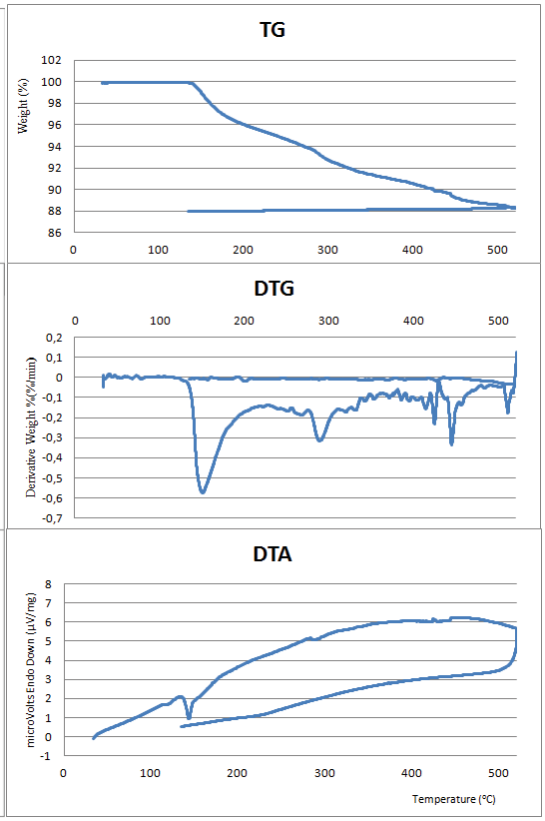
TG
Weight (%)
DTG
Derivative Weight %(%/min)
DTA
microVolts Endo Down (µV/mg)
Temperature (°C)

(b)

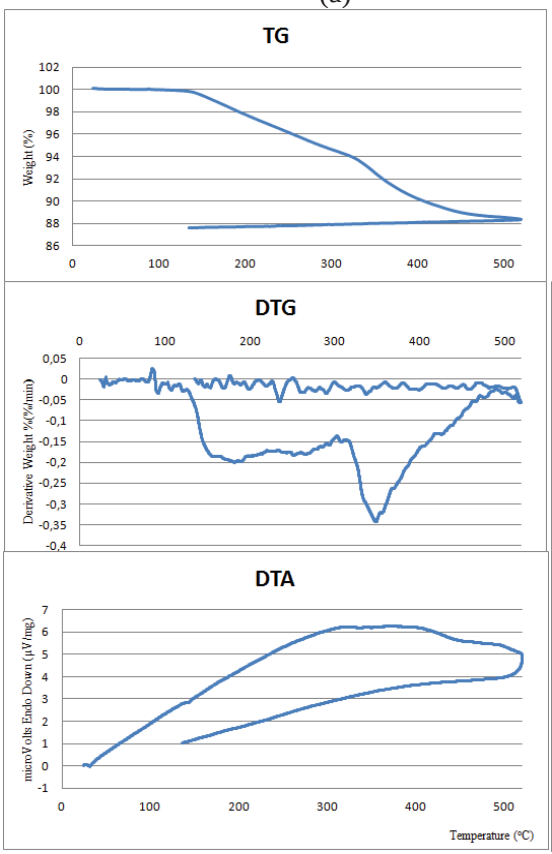
TG
Weight (%)
DTG
Derivative Weight %(%/min)
DTA
microVolts Endo Down (µV/mg)
Temperature (°C)

(c)

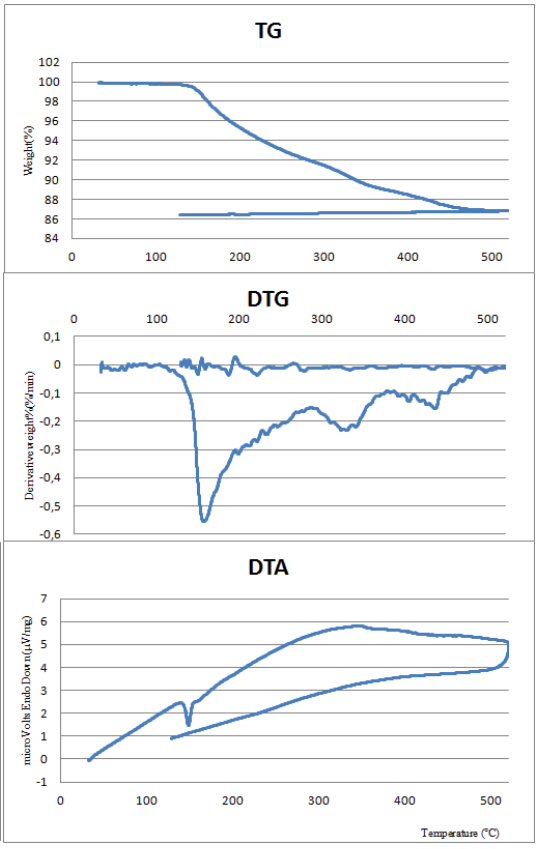
TG
Weight(%)
DTG
Derivativeweight%(%/min)
DTA
microVolts Endo Down(µV/mg)
Temperature (°C)

(d)

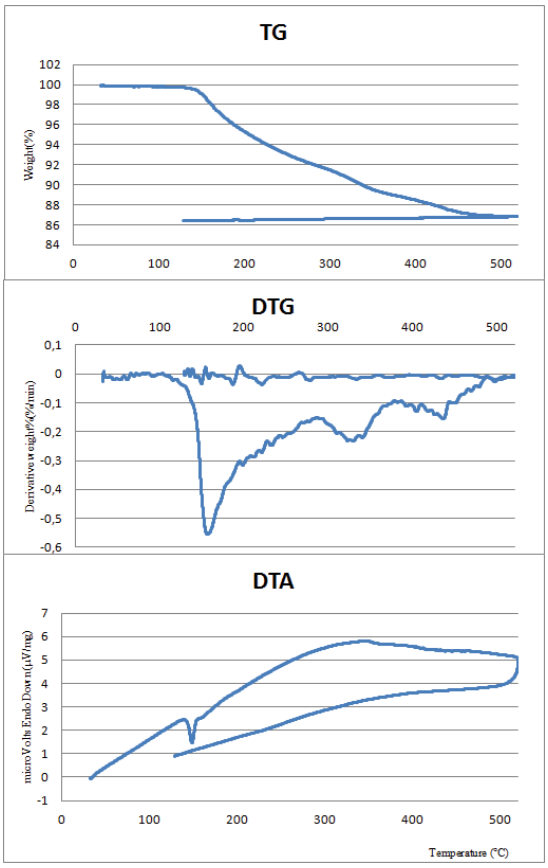

(e)

Figure 3: *TG, DTG and DTA analysis of the composites A, B, C, D and E*

4 Conclusion

Different compositions were synthesized and characterized for $xCsH_2PO_4 \cdot (1-x)Te(OH)_6$. The Ratio of $CsH_2PO_4/Te(OH)_6$ was found to be effective on thermal stability of the composites. The composite C with an equal molar amount of CsH_2PO_4 and $Te(OH)_6$ showed a promising thermal stability compared to CsH_2PO_4, which has a decomposition temperature of 200-230 °C. It seems that CsH_2PO_4 in the composite C does not decompose up to its melting point and this may give an opportunity for the composite C to be used as electrolyte up to its melting point.

Acknowledgement

The authors would like to thank Yıldız Technical University for the support of this study. This study is funded by Scientific Research Project Coordination of Yıldız Technical University (#2013-07-01-GEP02).

References

[1] A. Ikeda, S.M. Haile, The thermodynamics and kinetics of the dehydration of CsH_2PO_4 studied in the presence of SiO_2, Solid State Ionics, 213 (2012) 63-71.

[2] J. Otomo, T. Ishigooka, T. Kitano, H. Takahashi, H. Nagamoto, Phase transition and proton transport characteristics in CsH_2PO_4/SiO_2 composites, Electrochimica Acta, 53 (2008) 8186-8195.

[3] V.G. Ponomareva, E.S. Shutova, High temperature behavior of CsH_2PO_4 and CsH_2PO_4-SiO_2 composites, Solid State Ionics, 178 (2007) 729-734.

[4] J. Otomo, M. Minagawa, C.J. Wen, K. Eguchi, H. Takahashi, Protonic conduction of CsH_2PO_4 and its composite with silica in dry and humid atmospheres, Solid State Ionic, 156 (2003) 357-369.

[5] M. Dammak, H. Khemakhem, N. Zouari, A.W. Kolsi, T. Mhiri, Electrical properties of ferroelectric addition compound $K_2SeO_4 \cdot Te(OH)_6$, Solid State Ionics 127 (2000) 125–132.

Energy Efficiency Optimization of Superhydrophobic Surfaces for Enhanced Condensation Heat Transfer

K.J. Kubiak[a]*, Z. Khatir[b], P.K. Jimack[b], T.G. Mathia[c]

[a] University of Liverpool, School of Engineering, Liverpool L69 3GH, United Kingdom
[b] University of Leeds, School of Computing, Leeds LS2 9JT, United Kingdom
[c] Ecole Centrale de Lyon (LTDS), CNRS UMR 5513, 69134 Ecully, France
* Corresponding author. Email: k.kubiak@hud.ac.uk / kris@kubiak.co.uk; Tel.: +44 (0)148 447 1840

Abstract

The process of droplets jumping, against adhesive forces, from a solid surface upon coalescence has been studied in detail using experimentally-validated CFD modelling. Both Lattice Boltzmann and Volume of Fluid methods have been used to evaluate different kinematic conditions of coalescence inducing a jump velocity. Design of experiment techniques were used to establish near-optimal initial process parameters around which to focus the study. This multidisciplinary approach allows us to evaluate the jumping phenomenon for super-hydrophobic surfaces for which several input parameters may be varied, so as to improve the heat transfer exchange rate on the surface during condensation. Reliable conditions were found to occur for droplets within initial radius range of r=20-40 μm and static contact angle θ_s~160º. Moreover, the jumping phenomenon was observed for droplets with initial radius of up to 500 μm. Our study also shows that a critical contact angle for droplets to jump upon coalescence is θ_c~140º.

Keywords energy efficiency; heat transfer enhancement; drop-wise condensation; super-hydrophobic functional surfaces; multi-design optimisation.

1 Introduction

Drop-wise condensation processes, where condensation occurs through small droplets on a solid surface, has been demonstrated to significantly improve heat transfer rates in comparison to film-wise condensation (where a whole surface is covered by a thin film of liquid) [1]. Drop-wise condensation usually takes place on hydrophobic or super-hydrophobic surfaces as demonstrated by Boreyko and Chen [2]. One of the main technological challenges is to create such a surface, to allow condensation and evacuation of the droplets to take place in a continuous manner. Droplet coalescence is a complex physical phenomenon and optimisation of kinematic conditions leading to surface dewetting and jumping of droplets is of paramount importance for processes like heat transfer, atmospheric water harvesting or dehumidification [1]. Coalescence-induced jumping phenomena occur on superhydrophobic surfaces and within a small range of initial droplet radii. Recent interest in these phenomena has led to the influence of the droplets radii on the resulting jumping velocity to be explored [2, 3, 4]. In this study we investigate experimentally such jumping phenomena for larger droplets, in the range of 400μm and 500μm, and we develop numerical models to explore the effects of variation in initial droplet radius and the static contact angle of surface. We establish also a range of conditions where jumping upon coalescence can take place.

2 Experimental analysis and numerical modelling

Experimental results presented in this study, and previously published data by Boreyko et al. [2], are used to develop and validate two numerical models: a 2D Lattice Boltzmann (LB) and 3D Volume of Fluid (VoF) models. Our LB solver is based on the Shan-Chen [5] multiphase model, with wetting boundary conditions based upon the adhesion force proposed by Sukop and Thorne [6]. An advantage of the lattice Boltzmann method is that the interface between light and heavy fluids is diffuse, and the position of interface is computed as a result of the simulation. In particular, this approach does not require interface tracking or reconstruction. However, the modelled fluid can change phase and as it can be noticed in Figure 2 the air initially trapped between coalescing droplets compresses and change to a heavy phase (water). Unless otherwise stated, the following parameters were used in all of lattice Boltzmann simulations described in this work: G= -6, ρ_L=0.0734 ρ_H=0.0734, τ=0.54, $\delta x=2.5 \times 10^{-6}$m, $\delta t=2.86 \times 10^{-7}$s. These parameters correspond to water with surface tension σ=0.0727 N/m and dynamic

viscosity $\mu=4.3x10^{-3}$ Pa.s. A detailed description of this lattice Boltzmann solver may be found in [7]. The VoF solver uses similar physical parameters, and is based upon the OpenFOAM multiphase solver InterFoam [8], which is an interface-tracking technique. The VoF domain consists of the $[0, 2600\mu m]^3$ block discretised with 1M cuboid elements with: (i) no-slip imposed on the bottom, left and right walls for velocity, (ii) zero dynamic pressure and (iii) zero gradient on left and right walls with constant static angle equals to 157^o on the bottom wall for phase fraction.

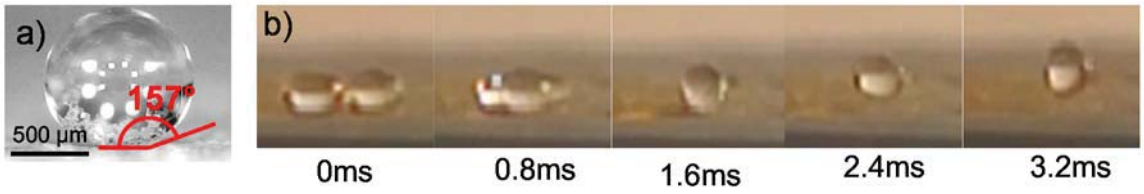

Figure 1: *Experimental validation of jumping phenomenon on superhydrophobic surface, (a) contact angle analysis, (b) droplet with initial radius 515 µm jumping upon coalescence, droplet velocity U=0.039 m/s*

For the physical experiments, the superhydrophobic surface has been prepared on copper alloy UNS C17000 by covering the surface with a thin layer of a paraffin film and subsequently by a layer of hydrophobic fumed silica. The prepared specimen was then heated to 50ºC to create a bond between the silica and paraffin films. Any excess silica powder was cleaned from the surface by a pressurised air jet. Such a prepared surface is superhydrophobic with a measured static contact angle of $\theta_s=157\pm2^o$ (Figure 1(a)).

To extend the range of experimentally explored conditions two droplets sizes were used which experience a jumping phenomenon upon coalescence: the initial radii being 405µm and 515µm. For each condition two droplets of the same size were carefully deposited on the superhydrophobic surface using a micro-pipette (0.2-2µl). Droplets were initially deposited in very close proximity so that even small vibrations can cause droplet movement and coalescence. The process was recorded with a high speed camera, with frame rate of 1200 fps. Examples of recorded droplets with initial radius of 515 µm are presented in Figure 1(b). The initial droplet velocities were measured by tracing the droplets' vertical position as a function of a time, and the slope of the resulting curve at the point when a droplet leaves the surface is taken as the initial jump velocity of that droplet. However, due to droplet oscillations, the vertical position of the droplet is calculated as the midpoint between the top and bottom droplet interface. This methodology was also used to calculate the initial droplet velocity in LB simulation. For VoF simulations, which were 3D in nature, using the lower interface position was found to give more reliable estimates of the coalescence-induced jump velocities however.

3 Results and discussion

As described above, the droplets' coalescence and jumping phenomena have been modelled numerically using both 2D LB (Figure 2) and 3D VoF (Figure 3) methods. Analysing the results of this numerical modelling, we believe that the primary jumping phenomenon can be explained as a dynamic process where the diameter of resulting droplet, following coalescence, is larger than the diameters of the initial droplets.

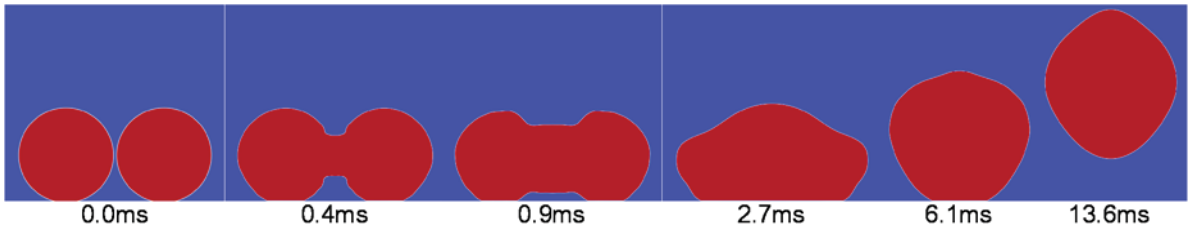

Figure 2: *Results of 2D LB modelling of droplet coalescence and jumping phenomenon, initial droplet radius 405 µm and droplet velocity U=0.064 m/s*

Kinetic momentum created initially by the coalescing droplets acts in horizontal direction, and deforms the interface, but the droplet can only escape upwards due to the close proximity of the solid wall (see the change of shape between 2.7ms and 6.1ms in Figure 2, and the change of shape between 0.8ms and 1.6ms in Figure 3 – note that the different time-scales is explained by the difference between 2D and 3D droplets). If the resulting vertical force, acting on the combined drop, is sufficient to overcome the adhesion forces between the surface and the droplet, the droplet will jump away from the surface. Viscous dissipation of the fluid will also take place. Further analysis concentrated on establishing necessary kinematic conditions for this jumping phenomenon to occur. A Design of Experiment approach was followed, with the initial droplet radius (r) and the static contact angle (θ_s) of the surface being analysed through 2D numerical simulations. The estimated surface response obtained from this analysis is presented in Figure 4.

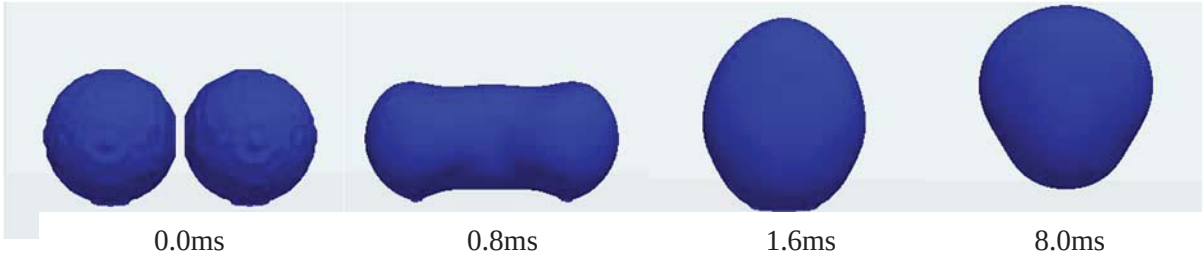

Figure3: *Results of 3D VoF modelling of droplet coalescence and jumping phenomenon, initial droplet radius 405 μm and droplet velocity U=0.005 m/s*

It may be noted that the jumping velocity is higher for more hydrophobic surfaces. This may be explained by the fact that the contact area between the merged droplet and the surface is smaller; therefore less energy is required to dewet the surface. Despite the expected advantage of more superhydrophobic surfaces, it is difficult to fabricate a long-lasting surface with static contact angle significantly above 160º. Hence, due to our desire for experimental validation, we focused our remaining simulations on surface with θ_s=160º. Analysing the initial droplet radius we conclude that the jumping velocity increases for smaller droplets with initial radius of about 30μm (Figure 4), however for smaller droplets (<20μm) the jump velocity follows experimental observations and decreases (see Figure 5(a), LB curve).

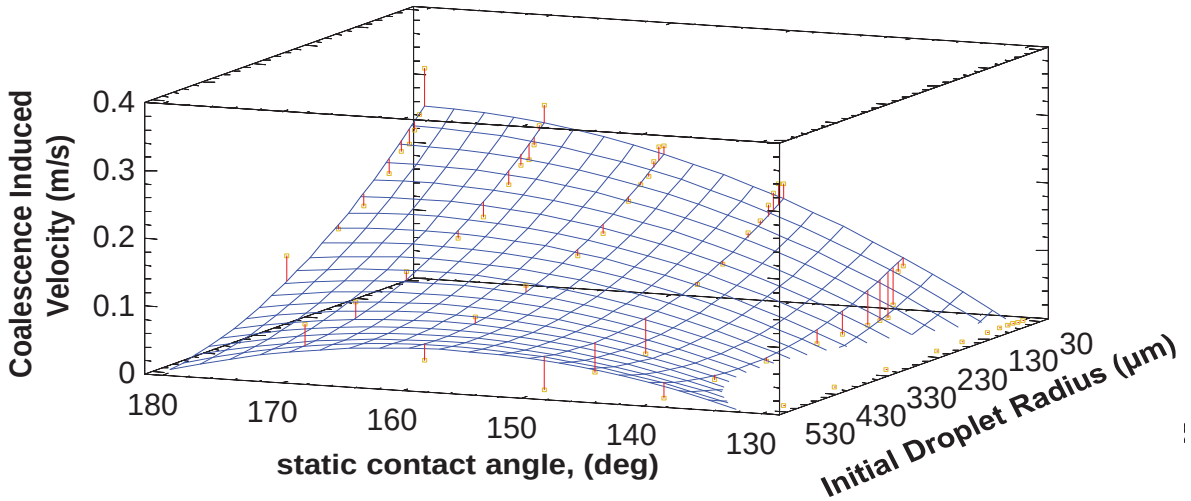

Figure 4: *Results of undertaking a surface response analysis of the jumping droplet velocity (m/s) as a function of static contact angle θ_s (º) and initial droplets radius R (μm)*

Figure 5(b) shows the influence of the static contact angle on the jumping velocity, and a critical value of the static contact angle has been obtained (θ_c=140º) for droplets with initial 2D radius of 100 μm. Jumping occurs for all values of θ_s between 140º and 180º. However, for a surface with static contact angle θ_s=160º, the jumping velocity is already 90% of the jumping velocity for θ_s=180º. A wider

selection of numerical results are presented in Figure 5(a), which shows very good agreement with experimental values across a wide range of initial droplet radii, from 20μm up to 500μm. Overall, the numerical methods developed in this study appear to show much more realistic predictions than the analytical model presented by Wang et al. [3] (Figure 5(a)). Note that we have fewer computation results for the 3D simulations undertaken by the VoF method [8]. These results are considerable more computationally demanding and are rather conservative in their estimates. This may be due to the difference in the point at which the jump velocity is computed for the 3D simulations. Further analysis will be required to understand the best way in which to compute this jump velocity, as well as any possible influence of surface morphology in 3D versus 2D simulations.

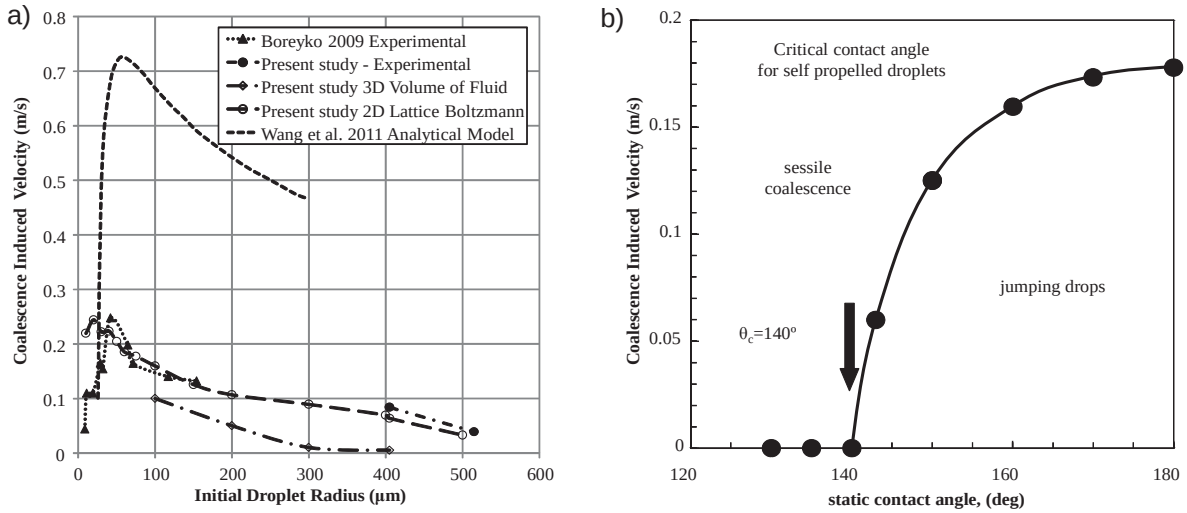

Figure5: *(a) Comparison of experimental and numerical results for the initial jumping velocity of droplets during coalescence on a superhydrophobic surface (θ_s=160°), (b) Influence of the static contact angle on the droplet jumping velocity, and determination of critical contact angle for jumping phenomenon (θ_c=140°) [Fig. b) after Khatir & Kubiak [9]]*

4 Conclusions

The process of droplet coalescence, and resulting jumping phenomena, have been successfully modelled numerically with both 2D lattice Boltzmann and 3D Volume of Fluid techniques. The coalescence-induced velocity of jumping droplets has been explored, and optimal kinematic conditions for jumping droplets have been established to be in a range of initial droplet radii from r=20μm to 40μm, for a static contact angle in the proximity of θ_s~160°. A critical contact angle for droplets to jump upon coalescence was estimated to be θ_c=140°. Further analysis, and additional full 3D modelling, will be required to complete the exploration of the range of fluid properties where jumping phenomena can occur. Furthermore, it would be desirable to include heat transfer optimization within the modelling capability. Nevertheless, even without optimization, it is clear that the development of functional surfaces to obtain continuous drop-wise condensation can be a good strategy to enhance the heat transfer rate in condensation processes.

References

[1] N. MiljkovicR. Enright, Y. Nam, K. Lopez, N. Dou, J. Sack, E.N. Wang, Jumping-Droplet-Enhanced Condensation on Scalable Superhydrophobic Nanostructured Surfaces, Nano Lett., 13 (1), 2013, 179-187.

[2] J.B. Boreyko, C.H. Chen, Self-Propelled Dropwise Condensate on Superhydrophobic Surfaces, Phys. Rev. Lett., 103, 2009, 184501.

[3] F.C. Wang, F. Yang, Y.P. Zhao, Size effect on the coalescence-induced self-propelled droplet, App. Phys. Lett. 98, 2011, 053112.

[4] B. Peng, S. Wang, Z. Lan, W. Xu, R. Wen, X. Ma, Analysis of droplet jumping phenomenon with lattice Boltzmann simulation of droplet coalescence, App. Phys. Lett. 102, 2013, 151601.

[5] X. Shan and H. Chen, Lattice Boltzmann model for simulating flows with multiple phases and components, Phys. Rev. E 47, 1993, 1815.
[6] M.C. Sukop, D.T. Thorne, Lattice Boltzmann modeling: an introduction for geoscientists and engineers, 2005, Springer Berlin.
[7] J.R. Castrejon-Pita, K.J. Kubiak, A.A. Castrejon-Pita, M.C.T. Wilson, I.M. Hutchings, Mixing and internal dynamics of droplets impacting and coalescing on a solid surface, Phys. Rev. E 88, 2013, 023023.
[8] S.S. Deshpande, L. Anumolu and M. F. Trujillo, Evaluating the performance of the two-phase flow solver InterFoam, Comput. Sci. Disc. 5, 2012, 014016.
[9] Z. Khatir, K.J. Kubiak, CFD based optimisation of the superhydrophobic functional surface in dropwise condensation, Proceedings of International Conference on the Analysis and Mathematical Applications in Engineering and Science (AMAES 2014), 19 – 22 January 2014, Curtin University Sarawak, Miri, Malaysia.

Adaptive Load Forecasting for Decentralized Co-generation Plant

Michael Short [a*], Muneeb Dawood [a], Tracey Crosbie [a] and Nashwan Dawood [a]

[a] Technology Futures Institute, Teesside University, Middlesbrough, TS1 3BA, UK
* Corresponding author. Email: m.short@tees.ac.uk

Abstract
Traditionally, for economic and safety reasons, most forms of energy worldwide have been generated by large centralized fossil-fuelled generators and transported to consumers via one-way transmission and distribution networks. However environmental concerns combined with the liberalization of the energy markets has forced a rethink in the way that energy is generated and distributed, leading to the emergence of small to medium-scale decentralised generation equipment embedded within the transmission and distribution networks. Commonly, such plant is operated by a small to medium private enterprise and dispatched independently from centralized resources. This paper focuses on short-term forecasting of both heat and electrical loads for a small/medium scale partially decentralized CHP plant. Such forecasting is required for the purposes of economic dispatch and efficient plant scheduling. An adaptive method is proposed to obtain reliable predictions over a future 'planning horizons' of around 24 hours. Results are presented in the form of a validation study illustrating the effectiveness of the approach using one year of representative plant data for a plant located in Angelholm, Sweden.

Keywords: short term heat and power load forecasting; decentralised CHP plant optimisation.

1 Introduction

Traditionally, for economic and safety reasons, the two most commonly consumed worldwide forms of energy – heat and electricity – have been generated by large fossil-fuelled generators and transported to consumers via one-way transmission and distribution networks (typically through hot water or steam pipe work and copper wires) [1]. Typically generation has been distributed over several large generating stations operating in parallel, with transmission interconnections spanning several countries, for electrical grids with these generators and interconnections under the control of a small number of public and private bodies [1, 2]. However the liberalization of the energy markets - combined with environmental concerns and the need for a low-carbon economy - has forced a rethink in the way that energy is generated and distributed to consumers [2]. In particular, the emergence of small- and medium-scale generation equipment (typically driven by renewable or alternative forms of energy conversion) embedded within the transmission and distribution networks is becoming increasingly commonplace. This paper is concerned with forecasting to provide reliable load predictions for scheduling a decentralized Combined Heat and Power (CHP) cogeneration plant to achieve economically efficient dispatch.

Cogeneration systems are broadly defined as the coincident generation of multiple forms of energy from a single fuel source: for CHP, the energy produced is the combined production of electric power and useable heat [3]. Cogeneration using CHP is an increasingly important component of energy production technology in Europe and other continents [3, 4]. Combined generation via CHP is highly efficient (typically ≅ 80%) when compared to a traditional power-only steam generator (typically ≅ 35% - 40%), and plant may be fired using a variety of sustainable low-carbon fuels, such as biomass [3]. This paper is concerned with a small/medium scale CHP plant which is serving a local load (heat and electricity) and operating in the presence of a wholesale energy market with fluctuating prices for the purchase and/or sale of electricity. The economic dispatch problem for such a plant can be stated as follows. Given a series of future hourly electrical and heat loads along with prices for buying /selling electricity and gas wholesale,, determine a plan for the hourly settings for CHP production, energy storage/retrieval and wholesale energy buying/selling that minimizes a weighted combination of economic and CO_2 emission costs [4]. The solution must also be subject to the natural constraints of the involved systems [4]. Clearly there are several factors which cannot be known accurately in such a formulation: the future heat and electricity loads and the wholesale energy prices being the principal examples. Therefore any optimization that takes place must employ predictions for these unknown quantities, typically

considering a future 'planning horizon' of 24 hourly steps [4]. This paper describes mathematical models and supporting software modules that developed to enable the operator of a CHP plant to automatically generate these hourly load predictions with minimum intervention. The load forecasting mechanisms have a simple structure but are adaptive in nature, employing Exponentially Weighted Recursive Least Squares (EWRLS) to efficiently obtain minimum variance predictions and track any environmental changes that would otherwise require manual model re-calibration. Results are presented in the form of a validation study illustrating the effectiveness of the approach using one year of representative data for a medium sized CHP plant located in Angelholm, Sweden. The remainder of this paper is organized as follows. Section 2 presents a framework for rolling horizon optimization and explains the role of the forecasting module. Section 3 discusses the load forecasting methods for heat and electricity, while Section 4 describes the test data and test results. A short conclusion is given in Section 5.

2 Rolling horizon optimization for CHP plant

The emergence of generation equipment embedded within energy transmission and distribution networks has helped to push forward the concept of the smart grid: an energy distribution network that not only allows for the physical transfer of energy but also features heavy automation and ICT support [2]. This ICT infrastructure offers many opportunities for improved monitoring, control and optimization of energy generation and distribution when compared to a traditional grid. One such improvement is the optimal economic balancing of energy supply with demand. The economic dispatch problem for a decentralized CHP plant must necessarily employ predictions for unknown loads and prices, and must also be reactive in the sense that when the state of the system evolves from one hour to the next and more reliable information is revealed, this information must be employed to update the previous dispatch plan to a better one. As such, the concepts of adaptive control (to track and adapt to changing conditions and supply/demand trends) [5] and receding-horizon predictive control (to re-calculate cost-optimal corrective strategies) [6] can be employed. A generic structure for such an optimization framework is as shown in Figure 1 below:

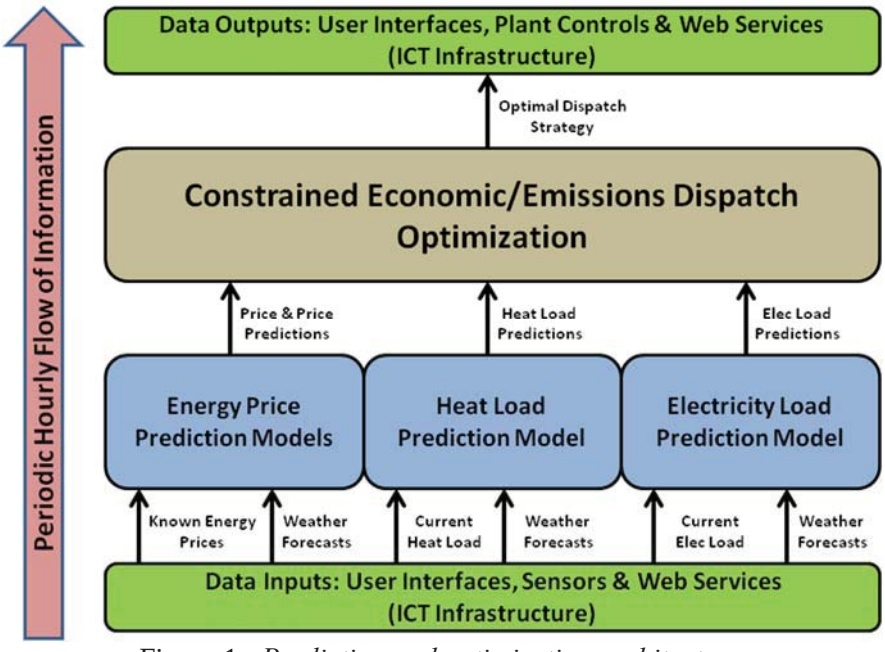

Figure 1: *Prediction and optimization architecture*

As can be seen in Figure 1, the data flow is periodic (typically with a one hour period); the operations highlighted require data acquisition to enable the prediction phase. In the data acquisition phase, measurements of the current state of the system (e.g. current loads) and related data (e.g. weather forecasts) are first acquired. Although this may be done manually, an underlying ICT platform is obviously preferred. The current and historical state measurements are then employed to predict the future energy demand evolution across the horizon along with the future wholesale market prices.

During the optimization phase, the optimal corrective strategy to balance supply and demand across the horizon using the available options for generating, storing, buying or selling energy are determined. During the post-processing phase, data extraction and post-processing is carried out and decision support information is then distributed locally or remotely (e.g. via email). Descriptions of a suitable PC-based ICT infrastructure to support such an optimization may be found in related work by the authors [7].

In a typical short-term energy market, there are three types of prices: day-ahead (spot) prices, intra-day (real-time) prices and regulation prices. At any point in time, only the intra-day (real-time) prices can be accurately known before market closure as they are advertised electronically in the exchange. Although spot prices are fixed once the market has closed and regulation prices are set retrospectively by the area TSO, forecasting methods may be employed [8, 9]. Information requirements for these forecasting models are typically historical prices, weather forecasts and information related to the wider status of the grid, e.g. volume of regulating power required. Predictions of hourly temperatures and wind speeds are often required: in the absence of specialised weather forecast information, free-to-use forecasting websites (e.g. www.yrno.api) can be utilized. In the following Section, adaptive models suitable for load forecasting of both electricity and heat loads for the CHP plant are presented. It is assumed that weather forecast information of the type above is available to these models.

3 Adaptive load and price forecasting

Previous observations suggest that for short-term heat and electricity prediction, simple but well-calibrated model structures often perform almost as well as complicated models (e.g. see [10, 11]), and strong load correlations with temperature can normally be found. A principal goal was therefore to keep the load prediction model structure very simple and to employ temperature as the only fundamental model input. In addition, to remove the need for extensive calibration and re-calibration of the model, a secondary goal was to use recursive adaptive parameter estimation for model parameter identification.

3.1 Load prediction model structure

Let the variable $D(t)$ represent the demand for electricity or heat (in kWh) on the CHP plant for the hour ending at time t, and the variable $T(t)$ represent the average ambient temperature for the hour ending at time t. Assuming that the demand has auto-regressive integrated white-noise 'dynamics' with temperature as a fundamental input, the model structure below is obtained:

$$A(z)D(t) = B(z)T(t) + \frac{e(t)}{\Delta} \quad (1)$$

In which $e(t)$ is a zero-mean white sequence, z^{-1} is the backshift (delay) operator, $\Delta = 1\text{-}z^{-1}$, $A(z)$ and $B(z)$ are polynomials in z^{-1} with A monic. The integrated white sequence means that the loads are effectively experiencing unknown disturbances that are akin to Brownian motion or a random walk. In particular, this provides resilience against non-constant means (which demand data seems to exhibit). In a separate study of representative data, it was found that the load ending at hour t was mostly correlated to the load ending at hours t-1, t-24 and t-168, i.e. one hour before, one day before and one week before [7]. This seasonal autoregressive behaviour is consistent with other studies [11]; although it has been suggested that there may also be monthly and/or yearly seasonal correlations [11], these were omitted from the current models for the sake of simplicity. In terms of the temperature correlations, we have found that in the heat model, the load ending at hour t is inversely correlated with the ambient temperature in the hour ending at time t and in the previous hour ending at time t-1. For electricity, the load is positively correlated mostly with the hour ending at t and less so with the previous hour; however for consistency in the model the previous hour is also included. Setting $\Delta D(t) = D(t) - D(t\text{-}1)$ and $\Delta T(t) = T(t) - T(t\text{-}1)$ as the first difference in the load and temperature respectively, incorporating the suggested structure of the A and B polynomials (1) may be written in the incremental form:

$$\Delta D(t) = a_1\Delta D(t-1) + a_2\Delta D(t-24) + a_3\Delta D(t-168) + b_1\Delta T(t) + b_2\Delta T(t-1) + e(t) \quad (2)$$

Since at time t, $E\{e(t+1)\} = 0$ and $D(t+1) = D(t) + \Delta D(t+1)$, the one-step head prediction equation for the above model using all information available up to and including time t becomes:

$$\hat{D}(t+1\,|\,t) = D(t) + a_1\Delta D(t) + a_2\Delta D(t-23) + a_3\Delta D(t-167) + b_1\Delta\hat{T}(t+1\,|\,t) + b_2\Delta T(t) \quad (3)$$

Where a hat upon a variable indicates its predicted value is to be used. A two-step ahead prediction can be formed from recursion upon (3):

$$\hat{D}(t+2\,|\,t) = \hat{D}(t+1) + a_1\Delta\hat{D}(t+1) + a_2\Delta D(t-22) + a_3\Delta D(t-166) + b_1\Delta\hat{T}(t+2\,|\,t) + b_2\Delta\hat{T}(t+1\,|\,t) \quad (4)$$

Similarly, *k*-step ahead predictions across the full horizon are obtained in an identical fashion, i.e. by recursion upon the load and load change predictions obtained up to step *k*-1.

3.2 Adaptive parameter updating

Since the distribution of $e(t)$ becomes approximately Gaussian for large sample sizes due to the Central Limit Theorem, the unknown model parameters a_1, a_2, a_3 and b_1, b_2 can be reliably estimated using minimum-variance (least squares) techniques. At each time step t, when the actual load from step t-1 becomes known, the parameters are first updated online in an identification step to minimize the following objective function J (the final weighted quadratic error):

$$J(t) = \sum_{i=0}^{t-1} \lambda^{(t-i)} \left(\Delta D(i) - \Delta\hat{D}(i)\right)^2 \quad (5)$$

With $0<\lambda\leq 1$ acting as an exponentially receding weighting factor known as the 'forgetting factor'. The parameter estimation can be efficiently carried out using the method of EWRLS as described by Astrom and Wittenmark [5], with a complexity that is quadratic in the number of regression parameters. Following the regression update to estimate the unknown co-efficients at time t using the available measured data, the predictions are then carried out recursively as detailed above.

4 Validation testing

The above procedures for adaptive prediction have been coded as modular, configurable C++ libraries. The EWRLS algorithm implementation is based upon the standard Kalman-filter style algorithm [5]. For testing and validation purposes, anonymized sets of hourly data have been obtained for the hourly load on a district heating plant and hourly temperature measurements for the year 2009 for a medium scale CHP plant located in Angelholm, Sweden [12]. In addition, electricity demands were obtained for the Sweden SW4 control area (in which Angelholm resides) from the Nordpool spot website. This latter data is publically available. The electricity data for the whole area have been scaled such that the average demand matches the 42 MW electrical capacity of the CHP plant. Table I below reports the Mean Absolute Percentage Error (MAPE) recorded over the entire year of data for 1-24 hour ahead heat and electricity predictions using this data. The average MAPE over the entire horizon was 7.855 % for heat predictions and 3.380 % for electricity predictions; such accuracy is good considering the simplicity of the proposed models, and is achieved through the adaptive capabilities of the EWRLS algorithm.

5 Conclusions

In this paper an adaptive method was proposed to obtain reliable predictions over a future 'planning horizons' of around 24 hours for the forecasting of both heat and electrical loads for a small/medium scale partially decentralized CHP plant. Results were indicative that the proposed approach is viable to be used for the purposes of economic dispatch and efficient scheduling of a medium sized CHP plant. Future work will involve further validation tests on the proposed models.

Table 1: *MAPE over a 24-hour prediction horizon for heat and electricity demand*

Step	MAPE(E)	MAPE(H)	Step	MAPE(E)	MAPE(H)	Step	MAPE(E)	MAPE(H)
1	1.015	4.069	9	3.333	8.401	17	4.015	8.172
2	1.556	5.839	10	3.460	8.389	18	4.056	8.133
3	1.947	6.872	11	3.569	8.365	19	4.084	8.103
4	2.280	7.512	12	3.665	8.341	20	4.127	8.084
5	2.567	7.922	13	3.755	8.314	21	4.178	8.075
6	2.811	8.171	14	3.841	8.288	22	4.212	8.071
7	3.008	8.320	15	3.903	8.254	23	4.265	8.089
8	3.179	8.387	16	3.964	8.214	24	4.340	8.137

Acknowledgements
This research described in this paper was carried out in the context of the IDEAS Collaborative Project (Grant Agreement No. 600071) which is co-funded by the European Commission, Information Society and Media Directorate General, under the Seventh Framework Programme (FP7), Cooperation theme three, "Information and Communication Technologies". The authors wish to acknowledge the commission for their support, the efforts of the partners, and the contributions of all those involved in IDEAS. The authors would also like to thank Henrick Gadd of Lund University, Sweden and the staff of Öresundskraft, Sweden for providing the raw meter reading data that was employed in this study. This co-operation is gratefully acknowledged.

References
[1] G. Masters, *Renewable and Efficient Electric Power Systems*. New Jersey: John Wiley & Sons, 2004.
[2] J. Ekanayake, N. Jenkins, K. Liyanage, J. Wu & A. Yokoyama. *Smart Grid: Technology and Applications*. Wiley-Blackwell, 2012.
[3] N. Petchers, Combined Heating, Cooling & Power Handbook: Technologies & Applications: An Integrated Approach To Energy Resource Optimization, The Fairmont Press, 2003.
[4] F. Salgado & P. Pedrero, Short-term operation planning on cogeneration systems: A survey, *Electric Power Systems Research*, Vol. 78, pp. 835–848, 2008.
[5] K.J. Astrom & B. Wittenmark, Adaptive Control: 2nd Edition. Addison-Wesley Publishing, 1995.
[6] E.F. Camacho & C. Bordons, *Model Predictive Control (2nd Edition)*, Springer Verlag, 2004.
[7] M. Short, M. Dawood, U. Shvadron, J. Ye, D. Gras & M. Ala-Juusela. Specifications for a neighbourhood energy management tool. Deliverable D3.2 of IDEAS project, November 2013. Available at http://www.ideasproject.eu.
[8] T. Kristiansen, Forecasting Nord Pool day-ahead prices with an autoregressive model, *Energy Policy*, Vol. 49, pp. 328-332, 2012.
[9] K. Skytte, The regulating power market on the Nordic power exchange Nord Pool: an econometric analysis, *Energy Economics*, Vol. 21, pp. 295-308, 1999.
[10] D. Dotzauer, Simple model for prediction of loads in district-heating systems. *Applied Energy*, Vol. 73, pp. 277-284, 2002.
[11] J.W. Taylor, Triple seasonal methods for short-term electricity demand forecasting, *European Journal of Operational Research*, Vol. 204, pp. 139-152, 2010.
[12] H. Gadd & S. Werner, Heat load patterns in district heating substations, *Applied Energy*, Vol. 108, pp. 176-183, 2013.